

## S1. Formaldehyde nitrogen ratio (FNR)

For discussion of ozone ( $O_3$ ) sensitivity to its precursors, the formaldehyde nitrogen ratio (FNR) (Jin and Holloway, 2015) is used to feature the  $O_3$  formation regime, with  $FNR < 1.0$  representing VOC-limited regimes,  $FNR > 2.0$  representing  $NO_x$ -limited regime, and FNR between 1.0 and 2.0 representing transitional regime. For model evaluation, monthly mean Aqua OMI tropospheric columns of nitrogen dioxide ( $NO_2$ ) (Boersma et al., 2018) and formaldehyde (HCHO) (De Smedt et al., 2015) products in 2015 are obtained from <https://www.temis.nl/airpollution/>, with resolutions of  $0.125^\circ \times 0.125^\circ$  and  $0.25^\circ \times 0.25^\circ$ , respectively. The satellite observations are interpolated into  $2^\circ \times 2.5^\circ$  resolution to be consistent with that of model outputs. Figure S7 evaluates the simulated present-day tropospheric columns of  $NO_2$  and HCHO in CpdEpd simulation by comparing with Aqua OMI satellite observations. The tropospheric columns of  $NO_2$  and HCHO levels are overestimated by  $4.4$  and  $1.1 \ 10^{15}$  molec  $cm^{-2}$  in EC and by  $1.8$  and  $0.7 \ 10^{15}$  molec  $cm^{-2}$  nationwide, respectively. We also compared the simulated surface  $NO_2$  concentrations with observations from CNEMC in Fig. S8. The model generally captured the observed monthly variation in surface  $NO_2$  concentrations in EC, NCP, and YRD, with R values of  $0.44$ - $0.70$ . The systematic low biases of surface  $NO_2$  concentrations in the GEOS-Chem model (NMBs ranging from -51.7% to -19.2% in this work) were also reported in previous studies (Qu et al., 2020; Qu et al., 2022; Fang et al., 2024), because of the lack of representation of the spatial gradients in  $NO_2$  observations within the coarse GEOS-Chem grid cells (Qu et al., 2022).

**Table S1. Information of climate models in CMIP6 used in this study.**

Model	N	Member_id (Historical/SSP1-1.9)
CanESM5	2	r1i1p1f1, r1i1p2f1
GFDL-ESM4	1	r1i1p1f1
GISS-E2-1-G <sup>a</sup>	3	r1i1p1f2, r1i1p3f1, r1i1p5f1
GISS-E2-1-H <sup>b</sup>	2	r1i1p1f2, r1i1p3f1
MIROC-ES2H	1	r1i1p4f2
MIROC-ES2L	1	r1i1p1f2
Total	10	

<sup>a, b</sup> GISS-E2.1-G and GISS-E2.1-H are coupled models of the GISS-E2.1 atmospheric model with the GISS and HYCOM ocean models, respectively.

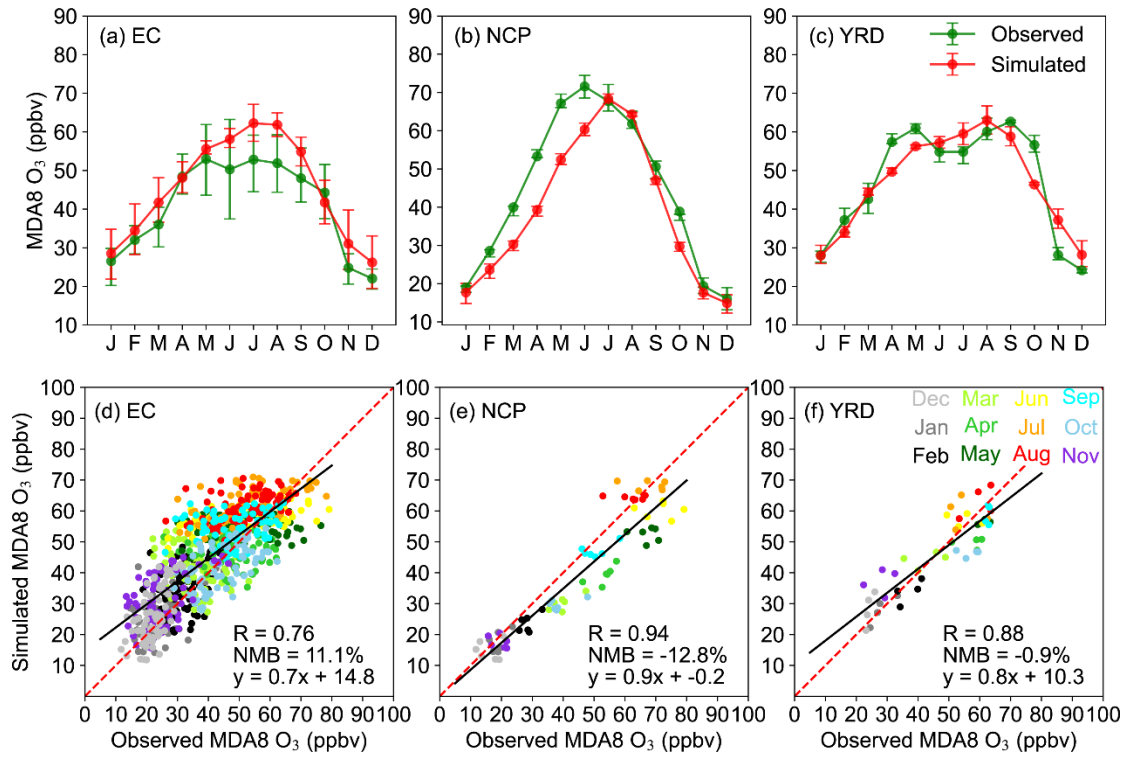


**Figure S1. (a)-(c)** Monthly variations in simulated and observed MDA8 O<sub>3</sub> concentrations (ppbv) over (a) EC (with a total of 68 grids), (b) NCP (with a total of 6 grids), and (c) YRD (with a total of 4 grids) regions. Bars represent the range from first to third quartiles of all grid samples in this region. (d)-(f) The scatterplot of simulated versus observed monthly mean MDA8 O<sub>3</sub> concentrations for grids in EC, NCP, and YRD. The linear fit (black solid line and equation), correlation coefficient (R), and normalized mean biases (NMB) that calculated for grids in these three regions are also shown when all of the year 2015 data are considered.

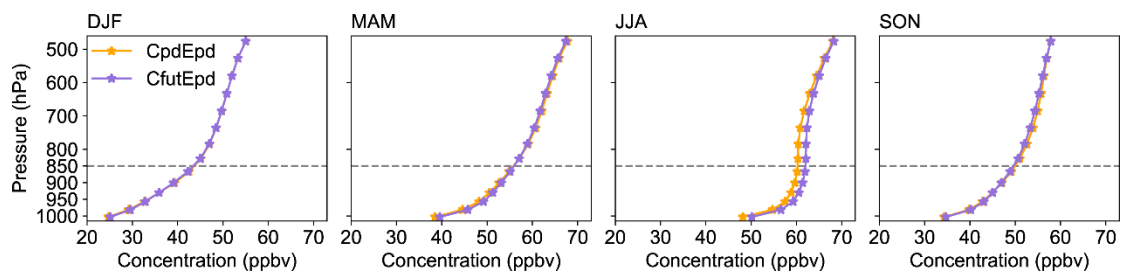


**Figure S2. Vertical profile of seasonal mean  $O_3$  concentrations (ppbv) over EC in CpdEpd and CfutEpd simulations.**

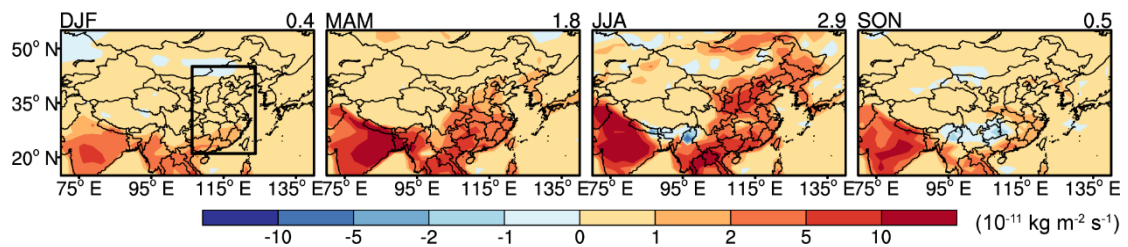


**Figure S3. Seasonal mean changes in biogenic emission rates of VOCs ( $10^{-11} \text{ kg m}^{-2} \text{ s}^{-1}$ ) due to climate change over 2010-2045. The black rectangle indicates the domain of EC, and the top right number of each panel is the regional mean value for EC.**

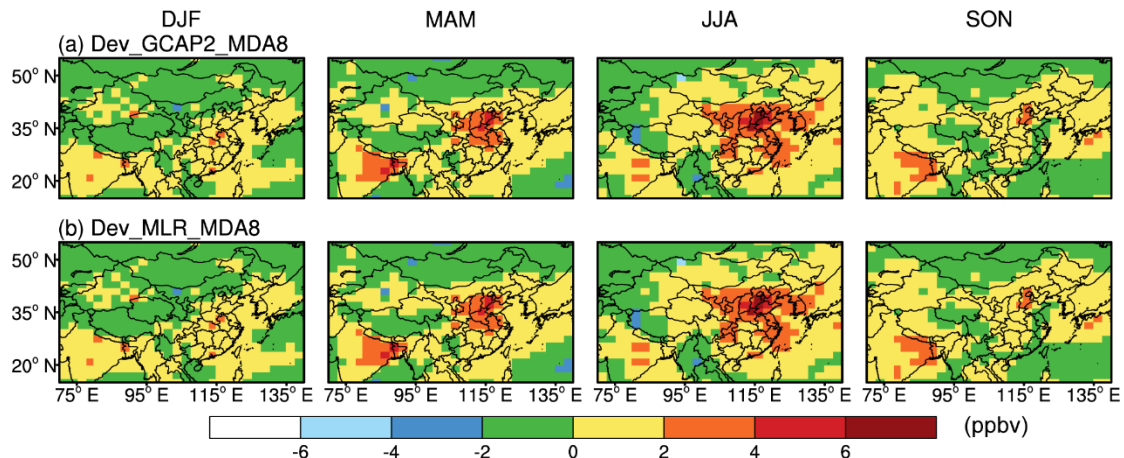


**Figure S4. Comparisons of the spatial distributions of climate-induced seasonal mean MDA8 O<sub>3</sub> changes simulated by (a) GCAP 2.0 (Dev\_GCAP2\_MDA8) with those predicted by (b) stepwise MLR model (Dev\_MLR\_MDA8).**

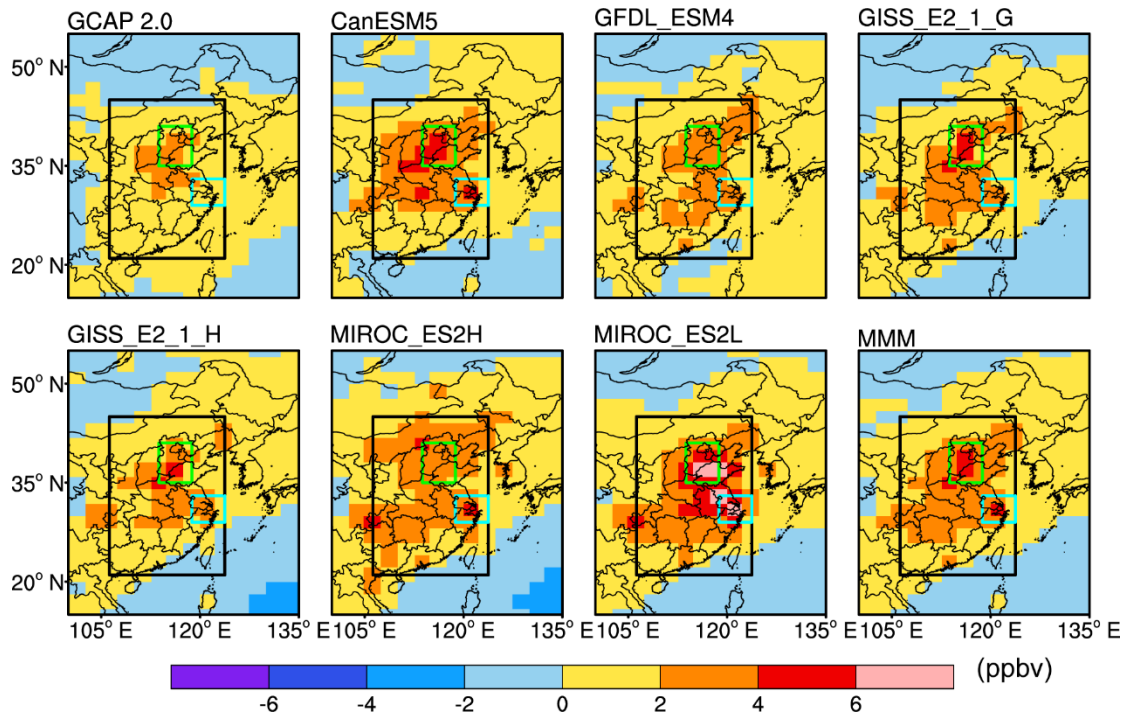


**Figure S5. The spatial distributions of climate-driven changes in annual mean MDA8 O<sub>3</sub> concentrations (ppbv) in EC projected by MLR model using the climate outputs from GCAP 2.0 and the other six CMIP6 models under SSP1-1.9 scenario. The multi-model mean (MMM) is calculated from the average of the six CMIP6 models.**

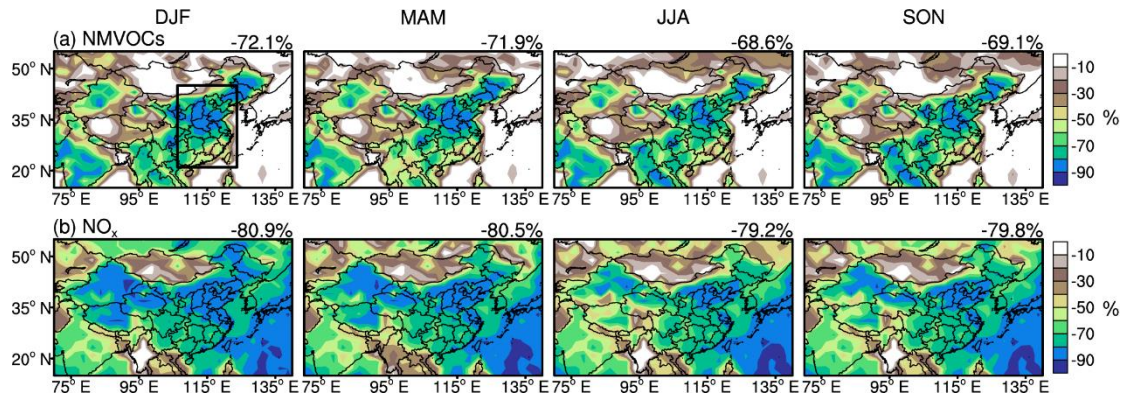


**Figure S6. Percentage changes (%) in anthropogenic emission rates of (a) NMVOCs and (b) NO<sub>x</sub> in 2050 relative to 2015 under SSP1-1.9 scenario. The black rectangle indicates the domain of EC, and the top right number of each panel is the regional mean value for EC.**

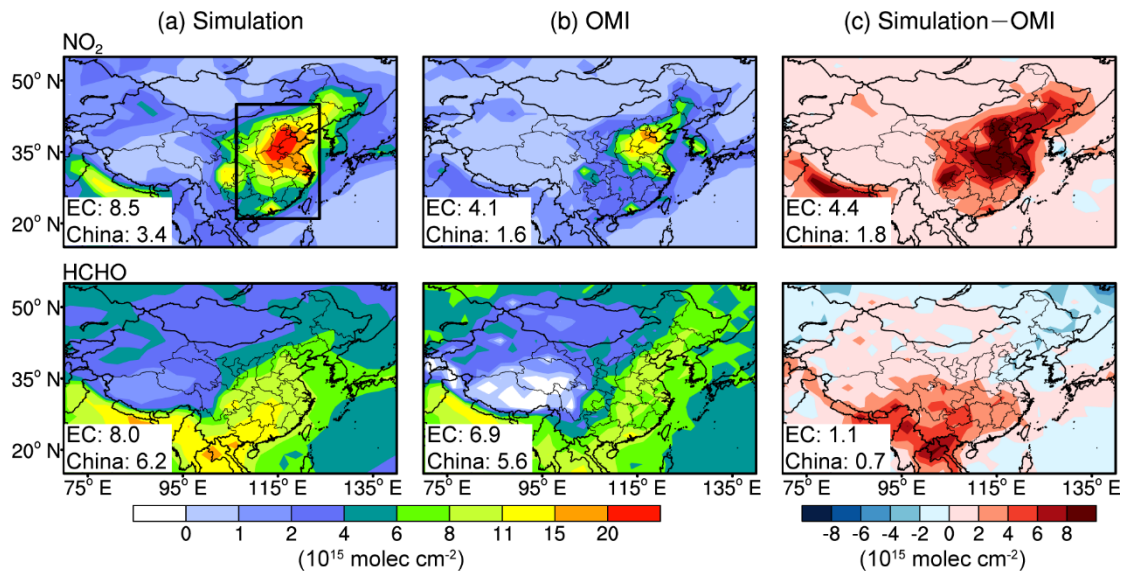


**Figure S7.** (a) Simulated and (b) OMI retrieved annual mean tropospheric columns of nitrogen dioxide (NO<sub>2</sub>) and formaldehyde (HCHO) ( $10^{15}$  molec  $\text{cm}^{-2}$ ) in 2015 in China, and (c) their difference. The black rectangle indicates the domain of EC, and the regional mean values for EC and the whole country are shown in the bottom left corner of each panel.

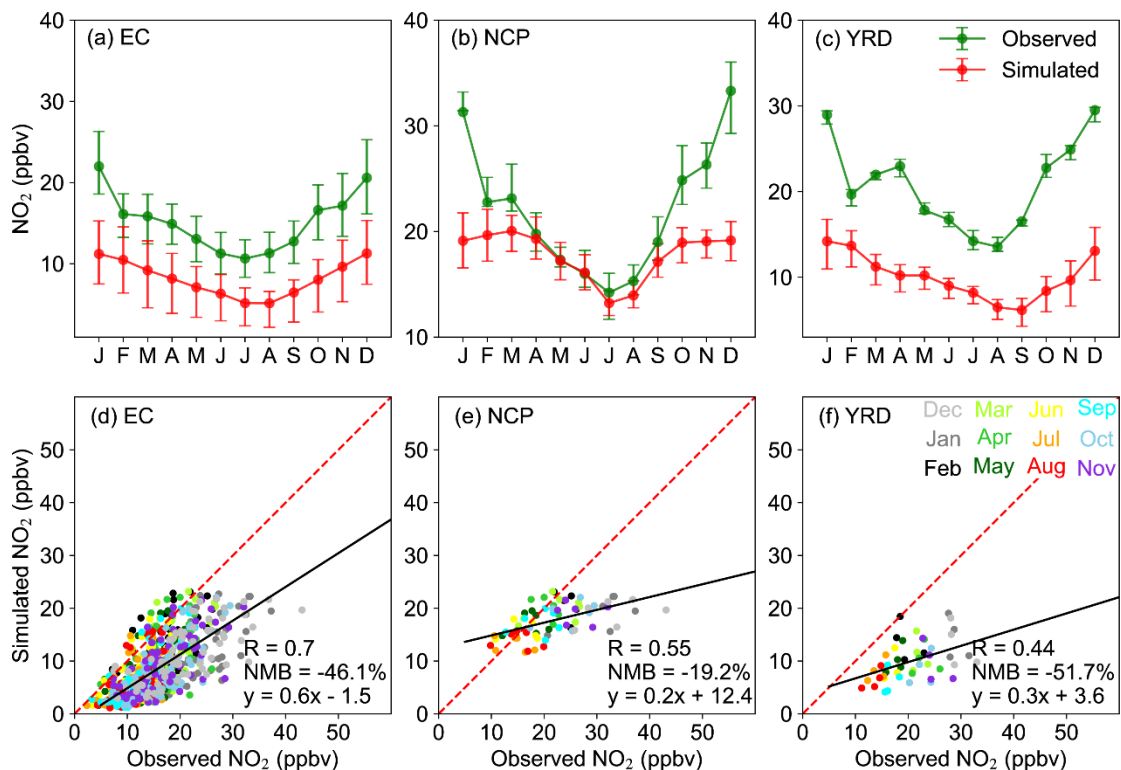


**Figure S8. (a)-(c)** Monthly variations in simulated and observed surface NO<sub>2</sub> concentrations (ppbv) over (a) EC (with a total of 68 grids), (b) NCP (with a total of 6 grids), and (c) YRD (with a total of 4 grids) regions. Bars represent the range from first to third quartiles of all grid samples in this region. (d)-(f) The scatterplot of simulated versus observed monthly mean surface NO<sub>2</sub> concentrations for grids in EC, NCP, and YRD. The linear fit (black solid line and equation), correlation coefficient (R), and normalized mean biases (NMB) that calculated for grids in these three regions are also shown when all of the year 2015 data are considered.

## References

Boersma, K. F., Eskes, H. J., Richter, A., De Smedt, I., Lorente, A., Beirle, S., van Geffen, J. H. G. M., Zara, M., Peters, E., Van Roozendael, M., Wagner, T., Maasakkers, J. D., van der A, R. J., Nightingale, J., De Rudder, A., Irie, H., Pinardi, G., Lambert, J.-C., and Compernolle, S. C.: Improving algorithms and uncertainty estimates for satellite NO<sub>2</sub> retrievals: results from the quality assurance for the essential climate variables (QA4ECV) project, *Atmos. Meas. Tech.*, 11, 6651-6678, <https://doi.org/10.5194/amt-11-6651-2018>, 2018.

De Smedt, I., Stavrakou, T., Hendrick, F., Danckaert, T., Vlemmix, T., Pinardi, G., Theys, N., Lerot, C., Gielen, C., Vigouroux, C., Hermans, C., Fayt, C., Veefkind, P., Müller, J. F., and Van Roozendael, M.: Diurnal, seasonal and long-term variations of global formaldehyde columns inferred from combined

OMI and GOME-2 observations, *Atmos. Chem. Phys.*, 15, 12519-12545, <https://doi.org/10.5194/acp-15-12519-2015>, 2015.

Fang, L., Jin, J., Segers, A., Li, K., Xia, J., Han, W., Li, B., Lin, H. X., Zhu, L., Liu, S., and Liao, H.: Observational operator for fair model evaluation with ground NO<sub>2</sub> measurements, *Geosci. Model Dev.*, 17, 8267-8282, <https://doi.org/10.5194/gmd-17-8267-2024>, 2024.

Jin, X. and Holloway, T.: Spatial and temporal variability of ozone sensitivity over China observed from the Ozone Monitoring Instrument, *J. Geophys. Res.: Atmos.*, 120, 7229-7246, <https://doi.org/10.1002/2015jd023250>, 2015.

Qu, Z., Henze, D. K., Cooper, O. R., and Neu, J. L.: Impacts of global NO<sub>x</sub> inversions on NO<sub>2</sub> and ozone simulations, *Atmos. Chem. Phys.*, 20, 13109-13130, <https://doi.org/10.5194/acp-20-13109-2020>, 2020.

Qu, Z., Henze, D. K., Worden, H. M., Jiang, Z., Gaubert, B., Theys, N., and Wang, W.: Sector-Based Top-Down Estimates of NO<sub>x</sub>, SO<sub>2</sub>, and CO Emissions in East Asia, *Geophys. Res. Lett.*, 49, <https://doi.org/10.1029/2021gl096009>, 2022.

1 **Effects of 2010-2045 climate change on ozone levels in China under**  
2 **carbon neutrality scenario: Key meteorological parameters and**  
3 **processes**

4 Ling Kang<sup>1</sup>, Hong Liao<sup>1\*</sup>, Ke Li<sup>1</sup>, Xu Yue<sup>1</sup>, Yang Yang<sup>1</sup>, Ye Wang<sup>2</sup>

5 <sup>1</sup> Jiangsu Key Laboratory of Atmospheric Environment Monitoring and Pollution Control, Jiangsu Collaborative Innovation  
6 Center of Atmospheric Environment and Equipment Technology, School of Environmental Science and Engineering, Nanjing  
7 University of Information Science & Technology, Nanjing 210044, China

8 <sup>2</sup> Key Laboratory of Meteorological Disaster, Ministry of Education (KLME)/Joint International Research Laboratory of  
9 Climate and Environment Change (ILCEC)/ Collaborative Innovation Center on Forecast and Evaluation of Meteorological  
10 Disasters (CIC-FEMD), Nanjing University of Information Science and Technology, Nanjing, China,  
11

12 *Correspondence to:* Hong Liao ([hongliao@nuist.edu.cn](mailto:hongliao@nuist.edu.cn))

13 **Abstract.** We examined the effects of 2010-2045 climate change on ozone ( $O_3$ ) levels in China under carbon neutrality  
14 scenario using the Global Change and Air Pollution version 2.0 (GCAP 2.0). In eastern China (EC), GCAP 2.0 and other six  
15 models from Coupled Model Intercomparison Projection Phase 6 (CMIP6) all projected increases in daily maximum 2-m  
16 temperature (T2max), surface incoming shortwave radiation (SW), and planet boundary layer height, and decreases in relative  
17 humidity (RH) and sea level pressure. Future climate change is simulated by GCAP 2.0 to have large effects on  $O_3$  even under  
18 carbon neutrality pathway, with summertime regional and seasonal mean MDA8  $O_3$  concentrations increased by 2.3 ppbv  
19 (3.9%) over EC, 4.7 ppbv (7.3%) over North China Plain, and 3.0 ppbv (5.1%) over Yangtze River Delta. Changes in key  
20 meteorological parameters were found to explain 58-76% of the climate-driven MDA8  $O_3$  changes over EC. The most  
21 important meteorological parameters in summer are T2max and SW in northern and central EC and RH in southern EC.  
22 Analysis showed net chemical production was the most important process that increases  $O_3$ , accounting for 34.0-62.5% of the  
23 sum of all processes within the boundary layer. We also quantified the uncertainties in climate-induced MDA8  $O_3$  changes by  
24 using CMIP6 multi-model projections of climate and a stepwise multiple linear regression model. GCAP 2.0 results are in the  
25 lower-end of the climate-induced increases in MDA8  $O_3$  from the multi-models. These results have important implications for  
26 policy-making regarding emission controls under the background of climate warming.

27 **1 Introduction**

28 Tropospheric ozone ( $O_3$ ) is a major secondary gas pollutant produced by the complicated photochemical reactions of  
29 methane ( $CH_4$ ), carbon monoxide (CO), volatile organic compounds (VOCs) and nitrogen oxides ( $NO_x$ ) in the presence of  
30 sunlight. It has adverse effects on human health (Lu et al., 2020; Li et al., 2021; Hong et al., 2019; Dang and Liao, 2019a),  
31 ecosystem (Yue et al., 2017; Grulke and Heath, 2020; Ainsworth et al., 2020), and climate (Checa-Garcia et al., 2018; Dang

32 and Liao, 2019a). Chinese government has implemented the Air Pollution Prevention and Control Action Plan since 2013,  
33 leading to large decline in NO<sub>x</sub> emissions and PM<sub>2.5</sub> concentrations (Zheng et al., 2018; Zhai et al., 2019), but O<sub>3</sub> pollution in  
34 eastern China (EC) became worse over the same time period (Tang et al., 2022; Li et al., 2020; Gong et al., 2020; Dang et al.,  
35 2021). Ozone pollution was particularly severe in the North China Plain (NCP), and observed summer mean maximum daily  
36 8-h average (MDA8) O<sub>3</sub> concentrations increased at a rate of 3.3 ppb yr<sup>1</sup> in NCP from 2013 to 2019, and reached 83 ppb by  
37 2019 (Li et al., 2020). Therefore, it is worth paying attention to the mid-to-long-term changes in O<sub>3</sub> concentrations in China in  
38 the future.

39 The projections of future climate or air quality rely on the future emission pathways under different socioeconomic  
40 scenario assumptions. Shared Socioeconomic Pathways (SSPs) are the state-of-the-art global emission scenarios, which  
41 combines socioeconomic and technological development with future climate radiative forcing outcomes into a scenario matrix  
42 architecture (Gidden et al., 2019). Gidden et al. (2019) constructed nine scenarios of future emissions trajectories, including  
43 SSP1-1.9, SSP1-2.6, SSP2-4.5, SSP3-7.0, SSP3-LowNTCF, SSP4-3.4, SSP4-6.0, SSP5-3.4-Overshoot (OS), and SSP5-8.5.  
44 Among all scenarios, only the SSP1-1.9 scenario achieves net negative emissions of carbon dioxide (CO<sub>2</sub>) for China and the  
45 world by 2060 (Wang et al., 2023), and thus we defined it as the carbon neutrality scenario and applied in this work. The SSPs  
46 scenarios are used in Scenario Model Intercomparison Project (ScenarioMIP) in Coupled Model Intercomparison Projection  
47 Phase 6 (CMIP6) to facilitate the integrated analysis of future climate impacts, vulnerabilities, adaptation, and mitigation  
48 (Gidden et al., 2019; Riahi et al., 2017).

49 Future O<sub>3</sub> concentrations depend on the future emissions. Shi et al. (2021) projected the O<sub>3</sub> concentration changes in  
50 China over 2020-2060 with no changes in meteorological conditions based on the Chinese Academy of Environmental  
51 Planning Carbon and Air Quality Pathways (CAEP-CAP) for pursuing the carbon neutrality. The 90<sup>th</sup> percentile of daily  
52 maximum 8-h average (MDA8) O<sub>3</sub> (90<sup>th</sup> MDA8 O<sub>3</sub>) in China reduced from 138  $\mu\text{g m}^{-3}$  in 2020 to 93  $\mu\text{g m}^{-3}$  in 2060 (a 33%  
53 reduction in 90<sup>th</sup> MDA8 O<sub>3</sub>). Based on Ambitious-pollution-Neutral-goals scenario from the Dynamic Projection model for  
54 Emissions in China (DPEC), Xu et al. (2022) used a regional climate-chemistry-ecology model to assess the impacts of regional  
55 emission reductions in China with the goal of achieving carbon neutrality by 2060, and found that the national average annual  
56 O<sub>3</sub> concentrations would decline by 35.6  $\mu\text{g m}^{-3}$  over 2015-2060. Wang et al. (2023) reported by using the GEOS-Chem model  
57 that the O<sub>3</sub> levels in Beijing-Tianjin-Hebei Region (BTH), Yangtze River Delta Region (YRD), Pearl River Delta Region  
58 (PRD), Sichuan Basin Region (SCB), and Fenwei Plain (FWP) under SSP1-1.9 scenario could meet the air quality standard  
59 by 2030, while those under SSP5-8.5 could not meet even by 2060. The 90<sup>th</sup> MDA8 O<sub>3</sub> in BTH, YRD, PRD, SCB, and FWP  
60 during 2015-2060 would change by -27.3%, -27.6%, -33.1%, -33.1%, and -31.8% under SSP1-1.9 scenario, and by +8.6%,  
61 +7.6%, +5.2%, -0.5%, and +2.9% under SSP5-8.5 scenario (Wang et al., 2023), respectively. However, these studies did not  
62 examine the effects of future climate change on O<sub>3</sub> concentrations.

63 Future O<sub>3</sub> concentrations also depend on future climate. Using the Weather Research and Forecasting Model with  
64 Chemistry (WRF-Chem) driven by Community Climate System Model version 3 (CCSM3), Liu et al. (2013) predicted that  
65 climate change caused a 1.6 ppb increase in surface O<sub>3</sub> over South China in October 2000-2050 under the IPCC A1B scenario.

66 They showed that future elevated near-surface temperature (1.6 °C) and increased emissions of isoprene (5-55%) and  
67 monoterpenes (5-40%) would lead to increases in chemical production of O<sub>3</sub>. By using GEOS-Chem model driven by NASA  
68 Goddard Institute for Space Studies (GISS) general circulation model (GCM) 3 under the A1B scenario, Wang et al. (2013)  
69 reported that climate change would cause a 0.55 ppbv increase in annual mean surface O<sub>3</sub> in EC over 2000-2050, in which  
70 more than 40% could be attributed to climate-induced increases in biogenic VOCs (BVOCs) emissions. Climate-induced  
71 increases in O<sub>3</sub> levels over EC **were** most pronounced and spatially extensive in summer, with a summer-average of 1.7 ppbv  
72 and a maximum of 10 ppbv. By employing a combination of models, Hong et al. (2019) projected that warm-season (April-  
73 September) averages of daily 1-h maximum O<sub>3</sub> levels would increase by 2-8 ppb in most of EC from 2006-2010 to 2046-2050  
74 under the Representative Concentration Pathway 4.5 (RCP4.5), in which 14% could be attributable to increased future heat  
75 wave days. Based on sensitivity simulations from five CMIP6 models by fixing sea surface temperatures (SSTs) at present-  
76 day or future conditions in the SSP3-7.0 scenario, Zanis et al. (2022) reported that the sensitivity of O<sub>3</sub> to temperature would  
77 enhance in regions close to anthropogenic sources or BVOCs emission sources (e.g., southern EC), with the values ranging  
78 from 0.2 to 2 ppbv °C<sup>-1</sup>. However, the scenarios utilized in these studies **were** not the representative scenarios in China in the  
79 context of carbon neutrality.

80 Few studies have examined the impacts of climate change under low-carbon or carbon-neutrality scenario. Li et al. (2023)  
81 showed that the annual mean surface O<sub>3</sub> during 2025-2095 increased by 0-2 ppb over EC under the SSP1-2.6 scenario by using  
82 a machine learning (ML) model along with multi-source data, with reduced relative humidity and enhanced downward solar  
83 radiation in the future favouring photochemical formation of surface O<sub>3</sub>. Zhu et al. (2024) investigated the effects of global  
84 and regional SSTs changes on surface O<sub>3</sub> levels in China during the warm season in 2050 (averaged over 2045-2054) based  
85 on global chemistry model simulations. They found that, compared with SSP5-8.5 scenario, future cooling of global ocean,  
86 North Pacific Oceans, and Southern Hemisphere oceans in SSP1-1.9 scenario would contribute to 0.79, 0.48, and 0.58 ppbv  
87 decreases in surface O<sub>3</sub> concentrations over EC, respectively, as a result of the weakened chemical production and anomalous  
88 upward airflow. However, these studies did not quantify the impacts of the dominant meteorological parameters and processes.

89 Climate change can influence tropospheric O<sub>3</sub> through altering meteorological fields and meteorology-sensitive physical  
90 and chemical processes. Integrated process rate (IPR) analysis, multiple linear regression (MLR) model and Lindeman,  
91 Merenda, and Gold (LMG) method are widely used to examine the contributions of main processes and key meteorological  
92 parameters to O<sub>3</sub> changes in China (Gong et al., 2022; Dang et al., 2021; Li et al., 2019). Liu et al. (2013) found that climate-  
93 induced changes in boundary layer O<sub>3</sub> budget were dominated by chemical processes, with gas-phase chemical reaction yield  
94 increasing by 3 ppb h<sup>-1</sup> in PRD over 2000-2050. The maximum increases in O<sub>3</sub> by chemical process were located in areas with  
95 significant warming as well as high anthropogenic and biogenic emissions of precursors. By combining MLR model and LMG  
96 method, Dang et al. (2021) showed that higher temperature and anomalous southerlies were key meteorological contributors  
97 to summer O<sub>3</sub> increases in NCP in 2017 relative to 2012, while weaker wind speeds and lower relative humidity were the key  
98 contributors in YRD. Gong et al. (2022) found by using the IPR analysis that net chemical production, diffusion, dry deposition,

99 horizontal advection and vertical advection during O<sub>3</sub> pollution events in 2014-2017 changed by 3.3, -1.1, -0.4, -9.1 and 8.1  
100 Gg O<sub>3</sub> d<sup>-1</sup> in North China relative to the seasonal mean values. The positive effects of net chemical production and vertical  
101 advection were associated with a typical weather pattern characterized by high daily maximum temperatures, low relative  
102 humidity, anomalous southerlies and divergence in the low troposphere, and anomalous downward airflow from 500 hPa to  
103 the surface. However, to our knowledge, no study has combined these approaches to quantify the roles of key meteorological  
104 parameters and associated processes in climate-induced changes in tropospheric O<sub>3</sub> levels in China under the carbon neutrality  
105 scenario.

106 In this study, based on the version 2.0 of the Global Change and Air Pollution (GCAP 2.0) model framework, we examine  
107 the effects of 2010-2045 climate change on O<sub>3</sub> levels in China under carbon neutrality scenario, focusing on the key  
108 meteorological parameters and processes for climate-induced O<sub>3</sub> changes by using the stepwise MLR model, LMG method  
109 and IPR analysis. The observations and CMIP6 data, numerical models and experiments, and statistical analysis methods are  
110 given in Sect. 2. Section 3.1 shows GCAP 2.0 projected climate change over 2010-2045 and the comparisons with other six  
111 CMIP6 model projections. Simulated present-day O<sub>3</sub> concentrations and model evaluation, and future tropospheric O<sub>3</sub> changes  
112 driven by 2010-2045 climate change are presented in Sect. 3.2. Section 3.3 quantifies the key meteorological parameters and  
113 processes for climate-induced O<sub>3</sub> changes. The climate-driven MDA8 O<sub>3</sub> changes predicted by stepwise MLR model using  
114 climate outputs from CMIP6 models are shown in Sect. 3.4. Section 3.5 examines briefly the effects of emission change alone  
115 on O<sub>3</sub> levels. The conclusions are presented in Sect. 4.

## 116 2 Data and methods

### 117 2.1 Observations

118 The real-time monitoring air quality data released by the China National Environmental Monitoring Center (CNEMC)  
119 became operational in 2013. O<sub>3</sub> concentrations are measured by the ultraviolet spectrophotometry method, following the China  
120 Environmental Protection Standards 'HJ 654-2013'  
121 (<https://www.mee.gov.cn/ywgz/fgbz/bz/bzwb/jcffbz/201308/W020130802491142354730.pdf>). We used hourly O<sub>3</sub>  
122 concentrations at 1479 sites nationwide in 2015 and converted the data unit from micrograms per cubic meter (μg m<sup>-3</sup>) to parts  
123 per billion per volume (ppbv). Data quality control went through the following steps: (1) negative or missing values were  
124 removed; (2) MDA8 O<sub>3</sub> concentration was calculated if there were at least 6 hours of valid data in each 8-hour period; (3) a  
125 site with more than 95% valid data in 2015 was retained (1047 sites after data quality control). For model evaluation, observed  
126 MDA8 O<sub>3</sub> concentrations were averaged over sites within each of the 2° latitude by 2.5° longitude model grid cell (with a total  
127 of 118 grids).

128 **2.2 Numerical models and experiments**

129 **2.2.1 GCAP 2.0 model framework**

130 GCAP 2.0 model framework is a one-way offline coupling between the version E2.1 of the NASA Goddard Institute for  
131 Space Studies (GISS-E2.1) GCM and the global 3-D chemical transport model GEOS-Chem (Murray et al., 2021). Both the  
132 GISS-E2.1 GCM and the GEOS-Chem models have a horizontal resolution of 2° latitude by 2.5° longitude with 40 vertical  
133 layers extending from the surface to 0.1 hPa.

134 GISS-E2.1 GCM participated in CMIP6 experiments was described in detail by Kelley et al. (2020) and Miller et al.  
135 (2021). GISS-E2.1 contributed several configurations to CMIP6, and Murray et al. (2021) used the atmosphere-only  
136 configuration with the prescribed sea surface temperatures to re-perform the simulation of “r1i1p1f2” variant label and  
137 archived the subdaily meteorological diagnostics necessary for driving GEOS-Chem, namely GCAP 2.0 meteorology. The  
138 GCAP 2.0 meteorology (<http://atmos.earth.rochester.edu/input/gc/ExtData/GCAP2/CMIP6/>) for driving GEOS-Chem model  
139 (version 13.2.1, [http://wiki.seas.harvard.edu/geos-chem/index.php/GEOS-Chem\\_13.2.1](http://wiki.seas.harvard.edu/geos-chem/index.php/GEOS-Chem_13.2.1)) only covered the periods of the pre-  
140 industrial era (1851-1860), the recent past (2001-2014), the near-future (2040-2049), and the end-of-the-century (2090-2099)  
141 for seven future scenarios.

142 Version 13.2.1 of the GEOS-Chem model has O<sub>x</sub>-NO<sub>x</sub>-hydrocarbon-aerosol tropospheric chemistry mechanism (Bey et  
143 al., 2001; Pye et al., 2009) with the updated stratospheric chemistry mechanism from NASA’s Global Modeling Initiative  
144 (GMI). Photolysis rates are calculated based on Fast-JX v7.0 scheme (Eastham et al., 2014). Aerosols influence tropospheric  
145 O<sub>3</sub> through heterogeneous reactions and the changes in photolysis rates (Lou et al., 2014; Li et al., 2019). Dry deposition is  
146 computed using a resistance-in-series model (Wesely, 1989) with a number of modifications (Wang et al., 1998). Vertical  
147 mixing in planetary boundary layer (PBL) is calculated by a nonlocal scheme (Lin and McElroy, 2010). Cloud convection is  
148 parameterized as a single plume acting under the mean upward convective, entrainment, and detrainment mass for each level  
149 of a model column as archived from the GCM (Murray et al., 2021).

150 **2.2.2 Emissions**

151 Global anthropogenic and biomass burning emissions of pollutants are from the SSP1-1.9 inventory, which has a monthly  
152 temporal resolution and a 0.5° spatial resolution. The anthropogenic emissions in SSPs are from nine sectors (including  
153 agricultural, energy, industry, transportation, residential and commercial, solvents production and application, waste,  
154 international shipping, and aircraft), and the biomass burning emissions are from four sectors (including agricultural waste  
155 burning, forest burning, grassland burning, and peat burning) (Gidden et al., 2019). Future anthropogenic and biomass burning  
156 emission are obtained from the integrated assessment model (IAMs) results for each SSPs scenario after harmonization  
157 (enabling consistent transitions from the historical data used in CMIP6 to future trajectories) and downscaling (improving the  
158 spatial resolution of emissions) (Gidden et al., 2019). The impacts of future climate change on biomass burning emissions  
159 (including wild fire emissions) are not considered.

160 The available emission years of SSPs inventory are 2015, 2020, 2030, 2040, 2050, 2060, 2070, 2080, 2090, and 2100.  
 161 Therefore, corresponding to the mid-term climate change, we chose 2015 and 2050 emissions to represent the present-day and  
 162 future emissions, respectively. Present-day (year 2015) and future (year 2050) anthropogenic and biomass burning emissions  
 163 are given in Table 1. Year 2050 anthropogenic and biomass burning emissions are based on the SSP1-1.9 scenario of CMIP6  
 164 experiments. The anthropogenic and biomass burning emissions of NO<sub>x</sub>, CO, and NMVOCs are 27.2, 161.8, and 24.8 Tg yr<sup>-1</sup>  
 165 in EC in 2015, respectively, and are projected to decrease by 80.0%, 63.2%, and 70.0% in 2050 relative to 2015, respectively.  
 166 These changes are larger than the decreases in global total emissions (64.1%, 52.3%, and 31.6%, respectively). The  
 167 anthropogenic emissions of sulfur dioxide (SO<sub>2</sub>), organic carbon (OC), and black carbon (BC) are projected to decrease by  
 168 95.3%, 67.1%, and 84.8% in EC, and by 79.9%, 69.1%, and 82.6% globally, respectively, while ammonia (NH<sub>3</sub>) emission  
 169 remains stable.

170 Table 1 also lists the climate-sensitive natural emissions, including lightning and soil emissions of NO<sub>x</sub> and biogenic  
 171 emissions of VOCs which are calculated online based on the GCAP 2.0 meteorology. Lightning and soil emissions of NO<sub>x</sub> are  
 172 calculated using the cloud-top height scheme of Price and Rind (1992) and the Berkeley-Dalhousie Soil NO<sub>x</sub> Parameterization  
 173 (BDSNP) scheme developed by Hudman et al. (2012), respectively. Biogenic VOCs (BVOCs) emissions are computed using  
 174 the Model of Emissions of Gases and Aerosols from Nature Version 2.1 (MEGAN v2.1) (Guenther et al., 2012). In present-  
 175 day, the lightning and soil emissions of NO<sub>x</sub> and biogenic emissions of VOCs are 0.6, 1.1, and 16.0 Tg yr<sup>-1</sup> in EC, respectively.  
 176 Note that VOCs from the biogenic sources (16.0 Tg yr<sup>-1</sup>) are comparable to those from the anthropogenic emissions (24.4 Tg  
 177 yr<sup>-1</sup>) in EC. Compared to 2015, lightning and soil emissions of NO<sub>x</sub> and the BVOCs emissions are predicted to increase by  
 178 8.8%, 5.6 %, and 15.5% in EC, respectively. **Changes in all natural emissions are calculated by using projected climate change,**  
 179 **which are considered as the effects of climate change.**

180 **Table 1. The annual anthropogenic, biomass burning, and natural emissions (Tg yr<sup>-1</sup>) for the present-day (year 2015) and the future**  
 181 **(year 2050) under SSP1-1.9 scenario. The domain of eastern China (EC) is 21.00°-45.00° N, 106.25°-123.75° E.**

		Global			Eastern China		
		2015	2050	Change (%)	2015	2050	Change (%)
NO <sub>x</sub>	Anthropogenic	119.82	36.27	-69.73	27.14	5.38	-80.18
	Biomass burning	13.74	11.72	-14.70	0.07	0.06	-14.29
	Lightning	20.25	21.13	4.35	0.57	0.62	8.77
	Soil	35.64	36.98	3.76	1.08	1.14	5.56
CO	Anthropogenic	608.00	188.74	-68.96	159.61	57.69	-63.86
	Biomass burning	328.44	258.18	-21.39	2.19	1.81	-17.35
NMVOCs	Anthropogenic	284.21	189.46	-33.34	24.41	7.14	-70.75
	Biomass burning	49.11	38.35	-21.91	0.34	0.28	-17.65
	Biogenic VOCs	941.17	1029.46	9.38	15.95	18.42	15.49
SO <sub>2</sub>	Anthropogenic	98.63	19.87	-79.85	20.67	0.98	-95.26

	Biomass burning	2.16	1.75	-18.98	0.02	0.01	-50.00
NH <sub>3</sub>	Anthropogenic	61.34	61.73	0.64	7.65	7.71	0.78
	Biomass burning	3.91	2.97	-24.04	0.03	0.03	0.00
OC	Anthropogenic	19.59	6.05	-69.12	4.26	1.40	-67.14
	Biomass burning	15.23	11.34	-25.54	0.12	0.09	-25.00
BC	Anthropogenic	7.99	1.39	-82.60	2.10	0.32	-84.76
	Biomass burning	1.75	1.41	-19.43	0.01	0.01	0.00

## 182 2.2.3 Numerical experiments

183 The GCAP 2.0 meteorology are available for four time slices: pre-industrial era (1851-1860), recent past (2001-2014),  
 184 near-future (2040-2049), and end-of-the-century (2090-2099). Considering the available GCAP 2.0 meteorology, 2005-2014  
 185 meteorology is used to represent the present-day climate (2010), and 2040-2049 meteorology under SSP1-1.9 scenario is used  
 186 to represent the future climate (2045). To examine the respective and combined effects of future changes in climate and  
 187 emissions on surface O<sub>3</sub> levels, four numerical experiments are set up (Table 2). The simulations of CpdEpd, CpdEfut, CfutEpd,  
 188 and CfutEfut represent, respectively, O<sub>3</sub> levels under present-day climate and emissions, present-day climate and future  
 189 emissions, future climate and present-day emissions, and future climate and emissions. Therefore, (CfutEpd minus CpdEpd)  
 190 or (CpdEfut minus CpdEpd) indicates the individual effect of climate change or emission change on O<sub>3</sub> concentrations, and  
 191 (CfutEfut minus CpdEpd) indicates the combined effect of climate and emission changes. To smooth out the noise of natural  
 192 climate variabilities, each simulation is conducted for 10 years after a 1-year spin-up. Unless otherwise noted, all the results  
 193 presented in this study are 10 yr averages of 2005-2014 or 2040-2049.

194 **Table 2. Experiment design.**

Description	Meteorological fields	Natural emissions	Anthropogenic emissions	Biomass burning emissions
CpdEpd	2005-2014	2005-2014	2015	2015
CpdEfut	2005-2014	2005-2014	2050	2050
CfutEpd	2040-2049	2040-2049	2015	2015
CfutEfut	2040-2049	2040-2049	2050	2050

## 195 2.3 Statistical analysis methods

### 196 2.3.1 Stepwise MLR model and LMG method

197 To identify meteorological variables that have a significant effect on climate-induced MDA8 O<sub>3</sub> changes, we applied  
 198 stepwise multiple linear regression (MLR) model to relate 10 yr daily MDA8 O<sub>3</sub> anomalies to 10 yr daily meteorological

199 parameter anomalies in the target region or each grid cell. The time series of 10 yr daily MDA8 O<sub>3</sub> anomalies are obtained by  
 200 (CfutEpd minus CpdEpd), and 10 yr daily meteorological parameter anomalies are obtained by subtracting 2005-2014 from  
 201 2040-2049. Nine meteorological variables are considered in the MLR analysis (Table 3), including daily maximum 2-m  
 202 temperature (T2max), relative humidity (RH), surface incoming shortwave radiation (SW), planet boundary layer height  
 203 (PBLH), precipitation (PREC), sea level pressure (SLP), and 850 hPa wind fields (U850, V850, and WS850). We first  
 204 correlated 10 yr daily MDA8 O<sub>3</sub> anomalies with 10 yr daily meteorological parameter anomalies, and excluded meteorological  
 205 variables that are not significantly correlated with MDA8 O<sub>3</sub> at the 95% confidence level. We then performed collinearity  
 206 statistics on the retained meteorological variables based on the variance inflation factor (VIF): the meteorological variable with  
 207 the largest VIF was sequentially excluded until the VIFs of all meteorological variables were less than 10. After these steps,  
 208 the reserved meteorological variables were read into the stepwise MLR model, which is in the following form (Li et al., 2019):

$$209 \quad y = \beta_0 + \sum_{k=1}^N \beta_k x_k + \text{interaction term} , \quad (1)$$

210 where  $y$  is the daily MDA8 O<sub>3</sub> anomalies,  $(x_1, \dots, x_N)$  are the  $N$  meteorological variable screened by stepwise MLR model,  
 211 and  $\beta_k$  is the regression coefficient for the  $k$ -th meteorological variable. The adjusted coefficient of determination ( $R^2_{\text{adj}}$ ) of  
 212 MLR equation represents the proportion of climate-induced MDA8 O<sub>3</sub> changes that can be explained by the changes in key  
 213 meteorological variables.

214 We then used the Lindeman, Merenda, and Gold (LMG) method (Grömping, 2006) to quantify the relative contribution  
 215 of each meteorological variable reserved in MLR equation. The LMG method decomposes the MLR model-explained total  
 216  $R^2_{\text{adj}}$  into non-negative individual  $R^2_{\text{adj}}$  contribution from each correlative regressor.

217 **Table 3. Meteorological variables considered in the statistical analysis.**

Abbreviation	Description
T2max	Daily maximum 2-m temperature (K) <sup>a</sup>
RH	Relative humidity (%) <sup>b</sup>
SW	Surface incoming shortwave radiation (W m <sup>-2</sup> ) <sup>a</sup>
PBLH	Planet boundary layer height (m) <sup>a</sup>
PREC	Precipitation (mm d <sup>-1</sup> ) <sup>a</sup>
SLP	Sea level pressure (hPa) <sup>a</sup>
U850	850 hPa zonal wind (m s <sup>-1</sup> ) <sup>b</sup>
V850	850 hPa meridional wind (m s <sup>-1</sup> ) <sup>b</sup>
WS850	850 hPa wind speed (m s <sup>-1</sup> ) <sup>c</sup>

218 <sup>a</sup>Temporal resolution is 1-hour

219 <sup>b</sup>Temporal resolution is 3-hour

220 <sup>c</sup>Calculated from the horizontal wind vectors (U850, V850)

221 **2.3.2 IPR analysis**

222 Integrated process rate (IPR) analysis is used to quantify the contributions of climate-driven change in physical and  
223 chemical processes to O<sub>3</sub> mass changes in different seasons in EC (21.00-45.00°N, 106.25-123.75°E). Five processes that  
224 influence O<sub>3</sub> levels are investigated, including net chemical production, PBL mixing, dry deposition, cloud convection, and  
225 horizontal and vertical advection transport, which jointly determine the O<sub>3</sub> mass balance. All of the processes are diagnosed at  
226 every timestep and then summed over each day. The contribution of each process was calculated following Eqs. (2) and (3)  
227 (Dang and Liao, 2019b):

228  $PC_{DIFF\_i} = PC_{CfutEpd\_i} - PC_{CpdEpd\_i}$  , (2)

229  $\%PC_{DIFF\_i} = \frac{PC_{DIFF\_i}}{\sum_i^n abs(PC_{DIFF\_i})} \times 100\%$  , (3)

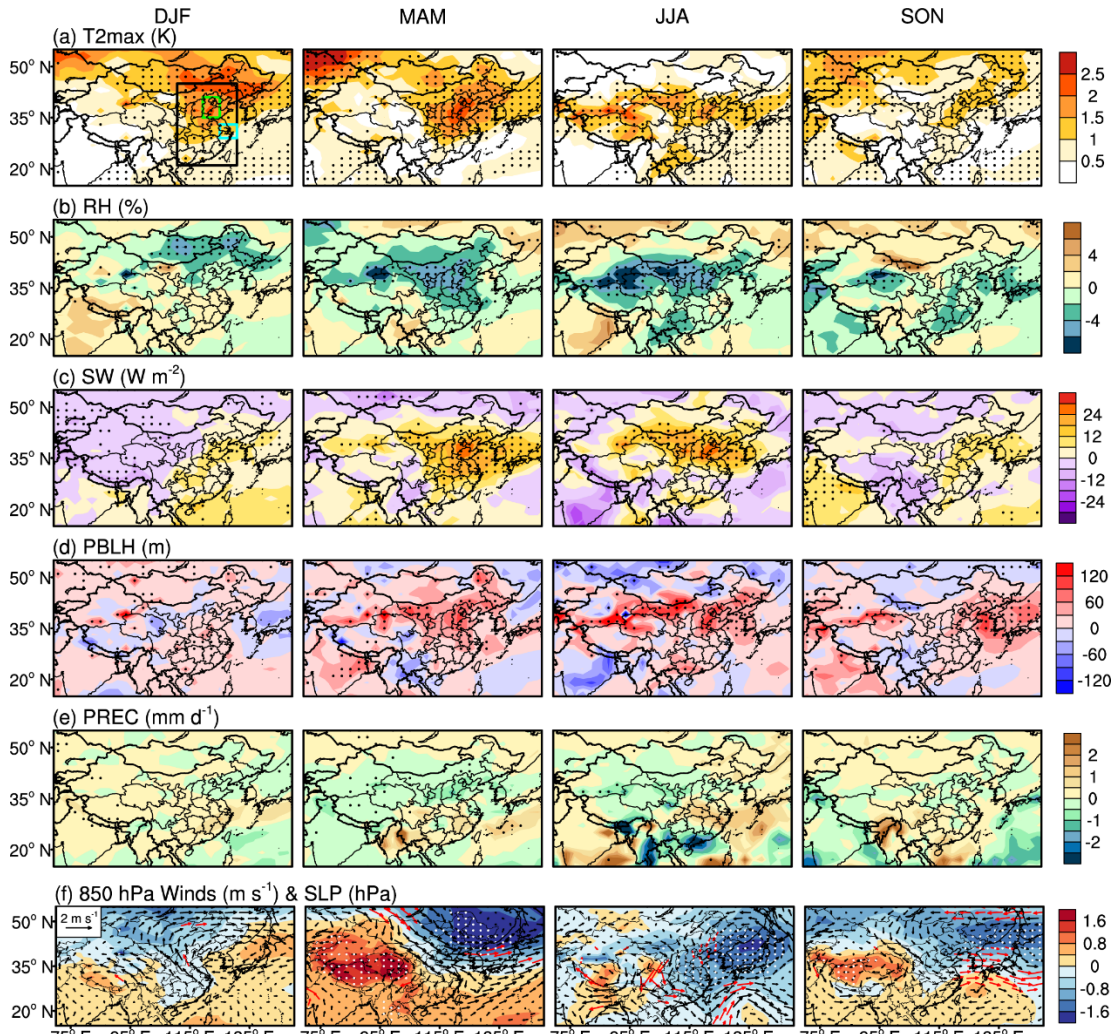
230 where  $n$  is the number of processes ( $n = 5$ ),  $PC_{CpdEpd\_i}$  and  $PC_{CfutEpd\_i}$  are the seasonal mean O<sub>3</sub> mass by process  $i$  from the  
231 CpdEpd and CfutEpd simulations, respectively, and  $PC_{DIFF\_i}$  is the climate-driven change in O<sub>3</sub> mass by process  $i$ .  $\%PC_{DIFF\_i}$   
232 is the proportion of process  $i$  in the total O<sub>3</sub> mass change caused by all processes. Note that the sum of absolute values of  
233  $\%PC_{DIFF\_i}$  for all processes equals 100%. The IPR analysis method has been widely used in previous studies to identify the  
234 key processes that contribute to air pollution episodes (Gong and Liao, 2019; Dai et al., 2023; Dang and Liao, 2019b) or drive  
235 the interannual and decadal variations in air pollutants (Yang et al., 2022; Mu and Liao, 2014).

236 **2.4 CMIP6 data**

237 The projected climate change by GCAP 2.0 may have uncertainties. To identify the range of uncertainties of the effects  
238 of climate change on MDA8 O<sub>3</sub>, we downloaded multi-model results of monthly means of the meteorological variables  
239 consistent with those in Table 3 in present-day (2005-2014) and future (2040-2049) under SSP1-1.9 scenario from the CMIP6  
240 data repository (<https://esgf-node.llnl.gov/search/cmip6/>). Since only six climate models in CMIP6 can provide PBLH, we  
241 selected outputs with the “r1” variant label from these models (Table S1). Note that GISS-E2.1-G and GISS-E2.1-H are  
242 coupled models of the GISS-E2.1 atmospheric model with the GISS and HYCOM ocean models, respectively, while the GCAP  
243 2.0 (or GISS-E2.1) is the atmosphere-only model with the prescribed sea surface temperatures. We extracted the monthly  
244 values for 2005-2014 and 2040-2049 from the raw data and interpolated them into GCAP 2.0 resolution (2° × 2.5°) by bilinear  
245 interpolation.

246 **3 Results**247 **3.1 Projected future climate change over China**248 **3.1.1 Projected climate change over 2010-2045 by GCAP 2.0**

249 Figure 1 shows the projected 2010-2045 changes in seasonal mean T2max, RH, SW, PBLH, PREC, U850 and V850, and  
250 SLP in winter (December-January-February, DJF), spring (March-April-May, MAM), summer (June-July-August, JJA), and  
251 autumn (September-October-November, SON) over China by GCAP 2.0 (or GISS-E2.1 GCM) under SSP1-1.9 scenario. The  
252 projected T2max, SW, and PBLH generally increase over EC while RH generally decreases. Regionally, the maximum  
253 increases in T2max occur in the northeastern China in DJF (2.0-2.5 K). The NCP (green rectangle in Fig. 1) has the largest  
254 temperature increases in other seasons, with values of 2.0-2.5 K in MAM, 1.5-2.0 K in JJA, and 1.0-1.5 K in SON. RH has a  
255 decrease of 2-6% over northern China in MAM and JJA, and of 2-4% over southern China in SON. Changes in SW and PBLH  
256 have similar spatial distributions, both of which increase largely over northern China in MAM and JJA. Precipitation generally  
257 increases over southeastern China in DJF and SON, and decreases in northern China in MAM. With respect to atmospheric  
258 circulations, over the Northwestern Pacific Ocean, there is an anomalous high-pressure in DJF and an anomalous low-pressure  
259 in other seasons. As a result, over EC, anomalous southerlies prevail in DJF and anomalous northwesterlies/northerlies prevail  
260 in other seasons.



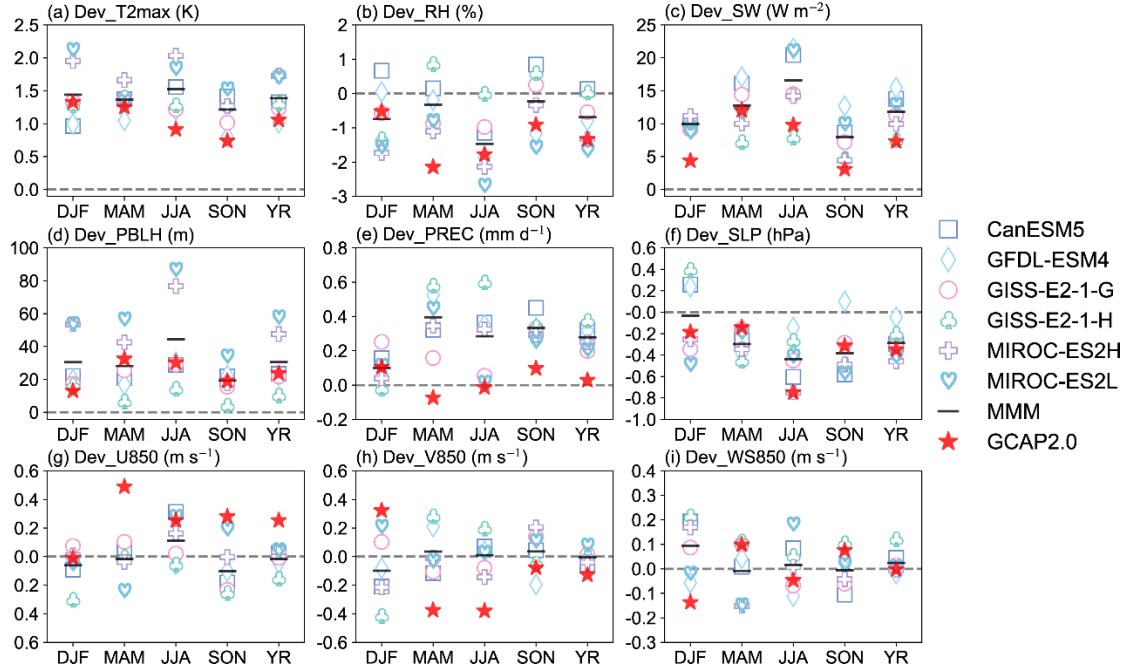
261

262 **Figure 1. Projected 2010-2045 changes in seasonal mean (a) daily maximum 2-m air temperature (T2max, K), (b) surface relative  
 263 humidity (RH, %), (c) surface incoming shortwave radiation (SW,  $\text{W m}^{-2}$ ), (d) planet boundary layer height (PBLH, m), (e)  
 264 precipitation (PREC,  $\text{mm d}^{-1}$ ), and (f) wind fields at 850 hPa (arrows,  $\text{m s}^{-1}$ ) and sea level pressure (SLP, shades, hPa) by GCAP 2.0  
 265 under SSP1-1.9 scenario. The dotted areas and red arrows represent a statistically significant difference at 95% confidence  
 266 according to Student's two sample t test. The black, green and blue rectangles in (a) indicate the domain of eastern China (EC, 21.00-  
 267 45.00°N, 106.25-123.75°E), North China Plain (NCP, 35.00-41.00°N, 113.75-118.75°E), and Yangtze River Delta (YRD, 29.00-33.00°N,  
 268 118.75-123.75°E), respectively.**

### 269 3.1.2 Comparisons with projected climate change from other CMIP6 models

270 The projected 2010-2045 changes in meteorological parameters (Table 3) under SSP1-1.9 scenario over EC by GCAP  
 271 2.0 are compared with those from six other CMIP6 models in Fig. 2. Increases in T2max, SW, and PBLH throughout the year  
 272 are robust features among all CMIP6 models. Most models projected reductions in RH and SLP and increases in PREC.

273 However, there are large model differences in winds at 850 hPa with inconsistent sign of changes. On a multi-model mean  
 274 (MMM) basis, projected annual mean changes over EC in T2max, SW, PBLH, PREC, RH, and SLP are 1.4 K,  $11.8 \text{ W m}^{-2}$ ,  
 275  $30.6 \text{ m}$ ,  $0.3 \text{ mm day}^{-1}$ ,  $-0.7\%$ , and  $-0.3 \text{ hPa}$ , respectively. Consistent with the MMM, the GCAP 2.0 projections show overall  
 276 increases in T2max, SW, PBLH, and PREC and decreases in RH and SLP, with the annual mean changes of 1.1 K,  $7.3 \text{ W m}^{-2}$ ,  
 277  $23.7 \text{ m}$ ,  $0.03 \text{ mm day}^{-1}$ ,  $-1.3\%$ , and  $-0.3 \text{ hPa}$ , respectively. Therefore, relative to the MMM, GCAP 2.0 underestimates the  
 278 increases in T2max, SW, PBLH, and PREC and overestimates the decreases in RH. The uncertainties in simulated future O<sub>3</sub>  
 279 caused by the uncertainties in future climate change will be quantified in Sect. 3.4.



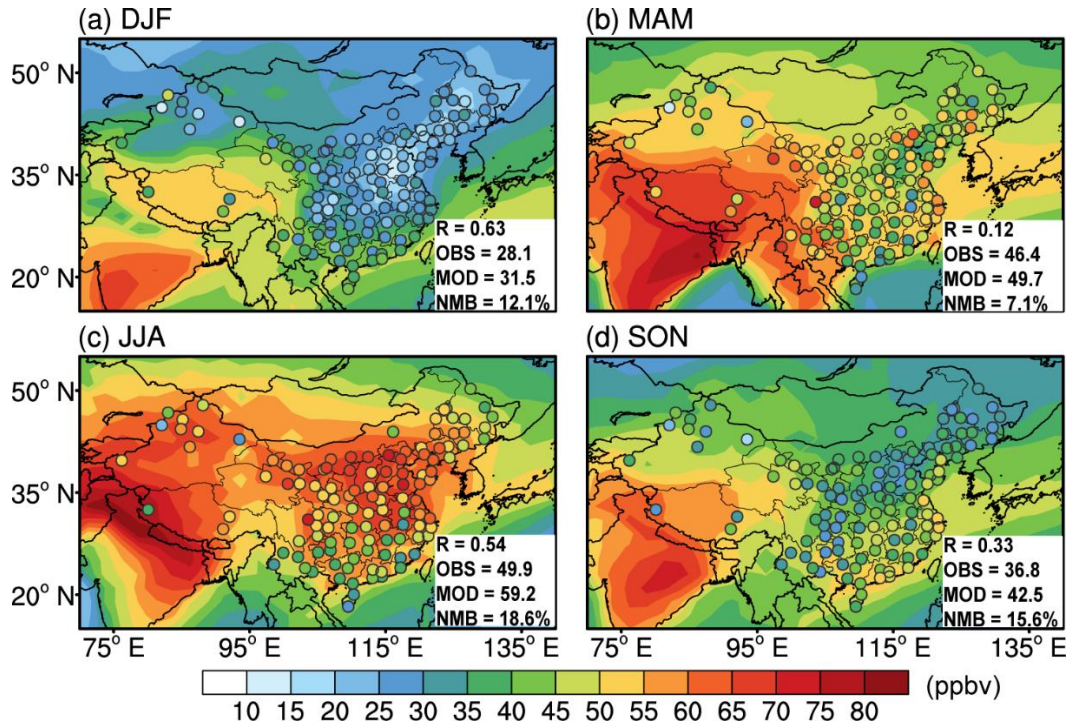
280 **Figure 2. Comparisons of simulated 2010-2045 changes in seasonal and annual mean meteorological parameters over EC by GCAP**  
 281 **2.0 with those by other six CMIP6 models under SSP1-1.9 scenario. Note that GISS-E2.1-G and GISS-E2.1-H are coupled models of**  
 282 **the GISS-E2.1 atmospheric model with the GISS and HYCOM ocean models, respectively, while the GCAP 2.0 (or GISS-E2.1) is**  
 283 **the atmosphere-only model with the prescribed sea surface temperatures. The multi-model mean (MMM) is calculated from the**  
 284 **average of the six CMIP6 models. Different markers represent different models, black lines represent MMM, and red stars represent**  
 285 **GCAP 2.0 results.**

## 287 3.2 Simulated present-day and future tropospheric O<sub>3</sub>

### 288 3.2.1 Present-day tropospheric O<sub>3</sub> and model evaluation

289 Figure 3 shows simulated present-day MDA8 O<sub>3</sub> concentrations from CpdEpd simulation and the observations in 2015  
 290 from CNEMC. We use 2015 observations to evaluate the simulated present-day MDA8 O<sub>3</sub> concentrations because emissions  
 291 of year 2015 are used for present-day. Simulated MDA8 O<sub>3</sub> concentrations in EC are highest in JJA (50-70 ppbv), followed

292 by MAM (35-55 ppbv), SON (30-50 ppbv), and DJF (10-45 ppbv). The model generally captures the spatial distributions of  
 293 the observed seasonal mean MDA8 O<sub>3</sub> levels over China, with spatial correlation coefficients (R) of 0.63, 0.12, 0.54, and 0.33  
 294 in DJF, MAM, JJA, and SON, respectively. Dang and Liao (2019a) also reported a low spatial correlation coefficient (R of  
 295 0.08) between observed and simulated seasonal mean O<sub>3</sub> in China in MAM of 2014-2017, which was attributed to the negative  
 296 biases in NCP and YRD whereas the positive biases outside these two regions. The model overestimates MDA8 O<sub>3</sub>  
 297 concentrations in China, with normalized mean biases (NMBs) of 7.1-18.6% in different seasons. Figure S1 shows monthly  
 298 variations in simulated and observed MDA8 O<sub>3</sub> levels over EC, NCP, and YRD. Both observed and simulated monthly mean  
 299 MDA8 O<sub>3</sub> concentrations are high during warm months (April-September) in these three regions. The NMBs in EC, NCP, and  
 300 YRD are 11.1%, -12.8% and -0.9%, respectively, which is consistent with results of Dang and Liao (2019a). The scattering  
 301 plots of model results vs. observations for grids in these three regions show correlation coefficients (R) of 0.76 to 0.94 when  
 302 all of the year 2015 data are considered.

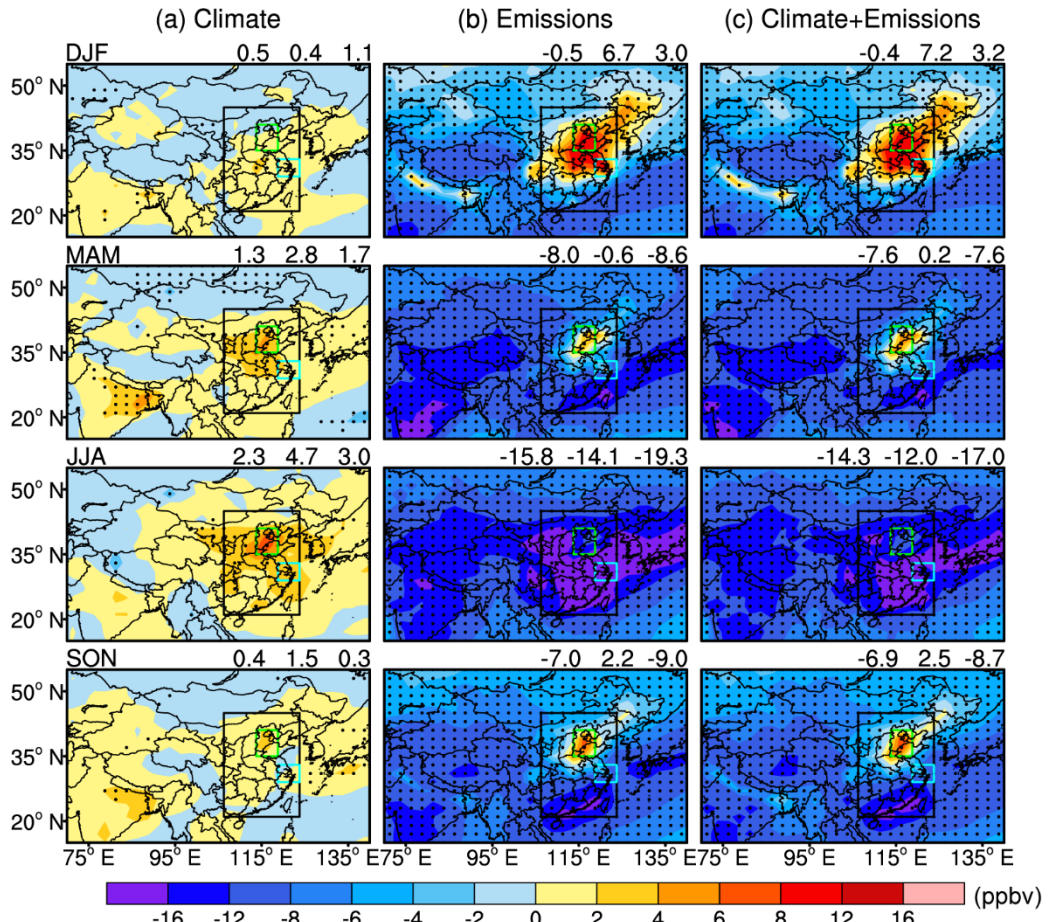


303  
 304 **Figure 3. Spatial distributions of observed (CNEMC, circles) and simulated (CpdEpd, shades) seasonal mean MDA8 O<sub>3</sub>  
 305 concentrations (ppbv) in 2015. Observed (OBS) and simulated (MOD) values that averaged over 118 grids, and their spatial  
 306 correlation coefficients (R) and normalized mean biases (NMB) are also shown at the bottom right corner of each panel.**

### 307 3.2.2 Future changes in tropospheric O<sub>3</sub> driven by climate change

308 Figure 4a shows future changes in seasonal mean MDA8 O<sub>3</sub> concentrations due to climate change (C<sub>future</sub>Epd minus  
 309 C<sub>present</sub>Epd). Climate change alone causes large increases in MDA8 O<sub>3</sub> values over EC in MAM and JJA, and the maximum value

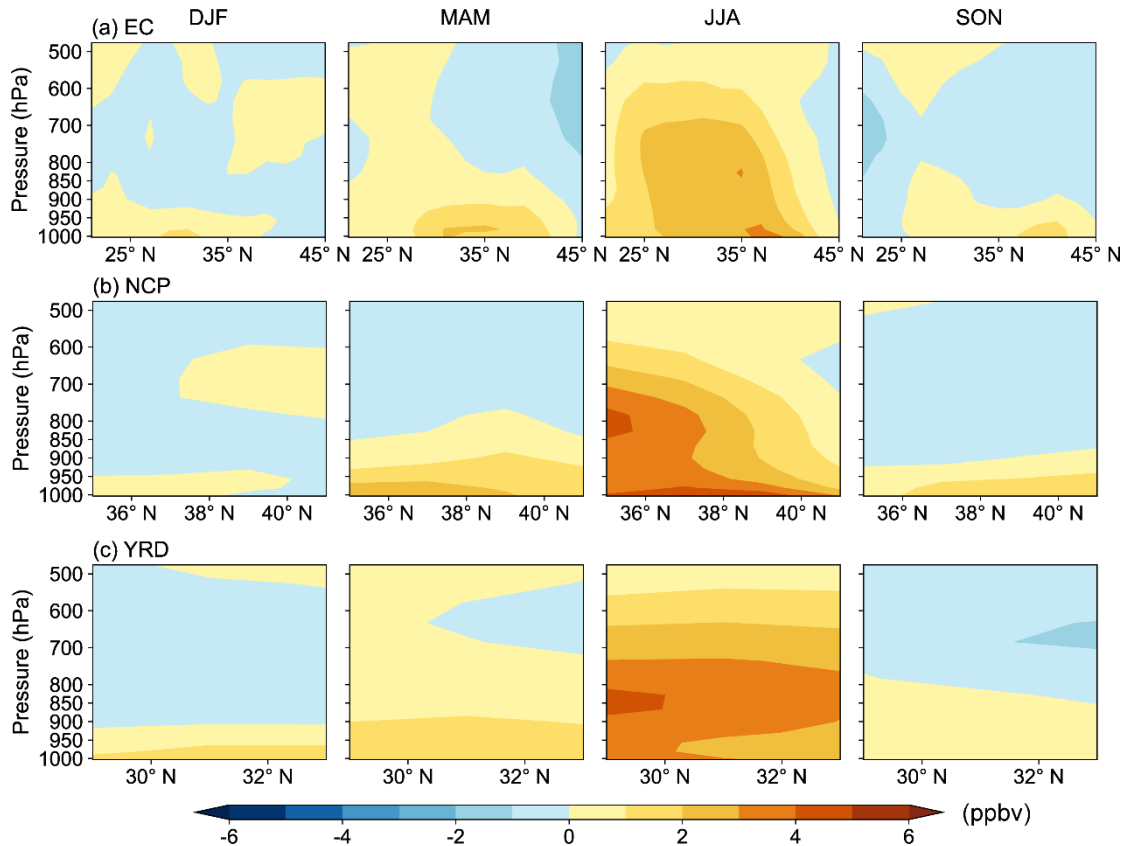
310 reaching 7.6 ppbv in NCP in JJA. In DJF, MAM, JJA, and SON, the regional and seasonal mean MDA8 O<sub>3</sub> values increase by  
 311 0.5 (1.5%), 1.3 (2.7%), 2.3 (3.9%), and 0.4 ppbv (1.0%) in EC, by 0.4 (2.0%), 2.8 (6.7%), 4.7 (7.3%), and 1.5 ppbv (4.6%) in  
 312 NCP, and by 1.1 (3.5%), 1.7 (3.3%), 3.0 (5.1%), and 0.3 ppbv (0.6%) in YRD, respectively. Our results are lower than the  
 313 recent study by Bhattacharai et al. (2024), who reported that climate change alone could lead to an increase of 5-15 ppbv in JJA  
 314 MDA8 O<sub>3</sub> levels in EC over 2010-2050 under SSP1-2.6 scenario by using Community Earth System Model (CESM) and  
 315 Community Atmospheric Model version 4 with chemistry (CAM4-chem).



316  
 317 **Figure 4. Predicted future changes in seasonal mean MDA8 O<sub>3</sub> concentrations (ppbv) due to (a) climate change alone (CfutEpd  
 318 minus CpdEpd), (b) emission change alone (CpdEfut minus CpdEpd), and (c) combined climate and emission changes (CfutEfut  
 319 minus CpdEpd) under SSP1-1.9 scenario. The black, green and blue rectangles indicate the domain of EC, NCP, and YRD,  
 320 respectively. The dotted areas represent a statistically significant difference at the 95% level according to Student's two sample t  
 321 test. The values at the top right of each panel are the regional mean values of EC, NCP, and YRD, respectively.**

322 The pressure-latitude cross sections of climate-driven seasonal mean O<sub>3</sub> changes from the surface to 500 hPa for EC,  
 323 NCP, and YRD are shown in Fig. 5. Vertically, O<sub>3</sub> increases of exceeding 1 ppbv extend from the surface to 500 hPa altitude

324 over the three regions in JJA. The maximum O<sub>3</sub> increases of 4-5 ppbv in NCP occur both at the surface and around 850 hPa,  
 325 and those of 3-5 ppbv in the YRD occur between 930 and 736 hPa. The O<sub>3</sub> increases over EC is large below 700 hPa over 25-  
 326 41°N, and the location of high values shifts from north to south with altitude, which is dominated by the pattern of NCP. In  
 327 other seasons, the O<sub>3</sub> increases of 1-3 ppbv are generally near the surface.



328  
 329 **Figure 5. The pressure-latitude cross sections of climate-driven seasonal mean O<sub>3</sub> changes (ppbv) averaged over the longitudes of (a)**  
 330 **106.25-123.75°E for EC, (b) 113.75-118.75°E for NCP, and (c) 118.75-123.75°E for YRD.**

331 **3.3 Key meteorological parameters and processes for climate-induced O<sub>3</sub> changes**

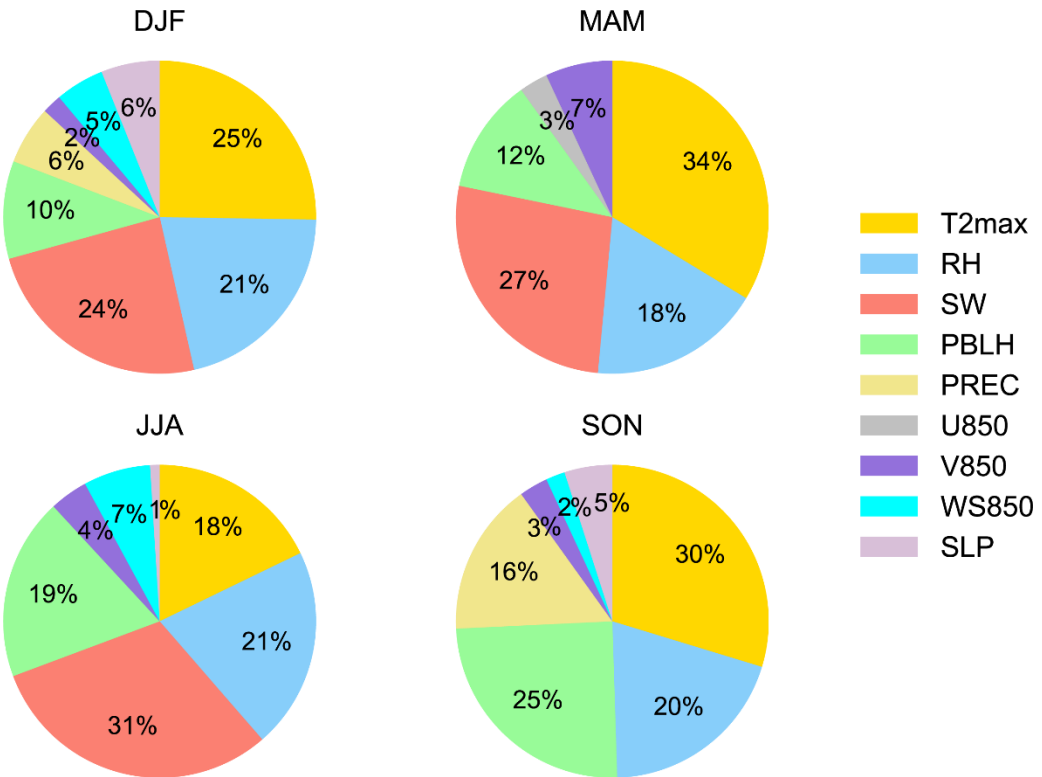
332 **3.3.1 Key meteorological parameters for climate-induced MDA8 O<sub>3</sub> changes**

333 For climate-induced changes in MDA8 O<sub>3</sub>, the stepwise MLR model is used to identify key meteorological variables that  
 334 have statistically significant effect on MDA8 O<sub>3</sub>, and the obtained R<sup>2</sup>\_adj represents the proportion of climate-induced MDA8  
 335 O<sub>3</sub> changes that can be explained by the changes in these key meteorological variables retained in MLR equation. Then, the  
 336 LMG method decomposes the MLR model-explained total R<sup>2</sup>\_adj and get the relative contribution of each meteorological  
 337 variable.

338 Table 4 shows the MLR equations between the daily anomalies of MDA8 O<sub>3</sub> and daily anomalies of meteorological  
 339 variables over EC for each season. The daily anomalies of both MDA8 O<sub>3</sub> and meteorological variables are 10 yr daily values,  
 340 which were derived from (CfutEpd minus CpdEpd) and ((2040-2049) minus (2005-2014)), respectively. For each key  
 341 meteorological variable, the positive or negative regression coefficient represents statistically significant positive or negative  
 342 effect of this variable on MDA8 O<sub>3</sub> concentrations. The R<sup>2</sup>\_adj of the MLR equations are 0.76, 0.74, 0.58, and 0.76 in DJF,  
 343 MAM, JJA, and SON, respectively, indicating 76%, 74%, 58%, and 76% of the climate-induced changes in MDA8 O<sub>3</sub> can be  
 344 explained by the changes in the key meteorological variables retained in MLR equations. Figure 6 shows LMG decomposed  
 345 contribution of each key meteorological variable in fitting climate-driven MDA8 O<sub>3</sub> changes over EC. The top three important  
 346 meteorological variables are T2max, SW, and RH, with the total contributions of 71.2% (T2max + SW + RH) in DJF, 78.2%  
 347 (T2max + SW + RH) in MAM, 70.1% (SW + RH + T2max) in JJA, and 49.9% (T2max + RH) in SON. PBLH is also a major  
 348 meteorological variable with the contributions of 9.6-24.5% in different seasons. The total contributions of the circulation  
 349 changes are 13.4% (SLP + WS850 + V850), 9.8% (V850 + U850), 11.4% (WS850 + V850 + SLP), and 9.5% (SLP + V850 +  
 350 WS850) in DJF, MAM, JJA, and SON, respectively.

351 **Table 4. Stepwise multiple linear regression (MLR) equations between the daily anomalies of MDA8 O<sub>3</sub> (CfutEpd minus CpdEpd)  
 352 and daily anomalies of meteorological parameters ((2040-2049) minus (2005-2014)) in EC. All the regression coefficients shown in  
 353 the equations passed the *t*-test of significance at 0.05 level.**

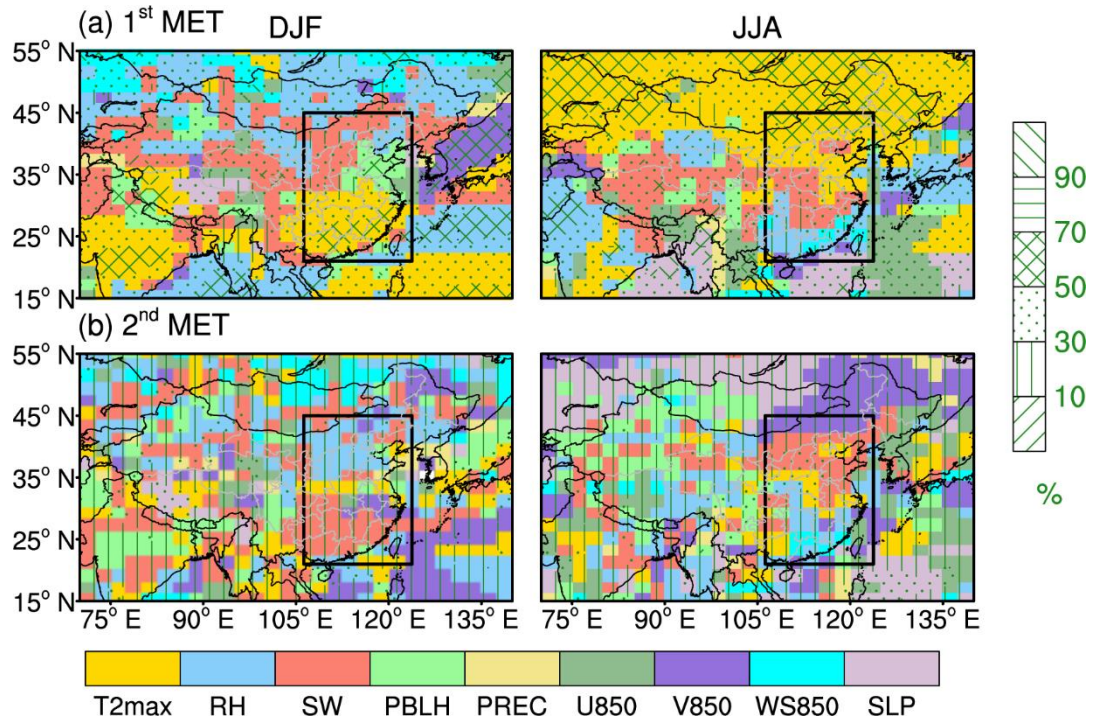
Season	Stepwise MLR equation	Adjusted coefficients of determination (R <sup>2</sup> adj)
DJF	MDA8 O <sub>3</sub> = -0.807 + 0.050*SW + 0.596*T2max + 0.016*PBLH + 0.247*PREC + 0.111*V850 + 0.066*SLP + 0.124*WS850 - 0.058*RH	0.76
MAM	MDA8 O <sub>3</sub> = -0.599 + 0.034*SW + 0.845*T2max + 0.324*V850 + 0.011*PBLH - 0.111*RH - 0.138*U850	0.74
JJA	MDA8 O <sub>3</sub> = 0.451 + 0.067*SW + 0.530*T2max + 0.552*V850 - 0.219*RH - 0.739*WS850 + 0.012*PBLH - 0.122*SLP	0.58
SON	MDA8 O <sub>3</sub> = -1.183 - 0.076*RH + 1.303*T2max + 0.035*PBLH - 0.370*WS850 + 0.151*V850 - 0.134*PREC + 0.066*SLP	0.76



354

355 **Figure 6. The LMG decomposed contribution (%) of each meteorological variable screened by stepwise MLR model in fitting**  
 356 **climate-driven MDA8 O<sub>3</sub> changes over EC. See Table 3 for the meanings of the abbreviations of meteorological variables.**

357 Large-scale regional average could obscure local characteristics, so we further conducted MLR and LMG analysis on  
 358 each grid cell to identify the first and second most important meteorological parameters (hereafter called “1<sup>st</sup> MET” and “2<sup>nd</sup>  
 359 MET”) in China as shown in Fig. 7. In DJF, the 1<sup>st</sup> MET is T2max in southern EC and is SW or PBLH in northern EC, which  
 360 has the relative contributions of 30-70% from LMG analyses. In JJA, the 1<sup>st</sup> MET is T2max in most parts of northern EC (north  
 361 of 36°N), SW in most parts of central EC (26-36°N), Beijing, and Tianjin, and RH and WS850 in southern EC (south of 26°N).  
 362 In the corresponding areas, T2max and SW have relative contributions of 30-70% and RH has relative contributions of 10-  
 363 30%. The regional heterogeneity of the 2<sup>nd</sup> MET increases compared to the 1<sup>st</sup> MET. In DJF, the 2<sup>nd</sup> MET is RH in northern  
 364 EC and SW in southern EC, with relative contributions of 10-30%. In JJA, the 2<sup>nd</sup> MET is mainly SW or T2max in northern  
 365 EC and RH or WS850 in southern EC. The relative contribution of 2<sup>nd</sup> MET (SW or T2max) in central EC can have relative  
 366 contributions of 30-50% in JJA. In summary, the key meteorological parameters for climate-induced MDA8 O<sub>3</sub> changes are  
 367 not only temperature, but also SW, RH, and PBLH, depending on locations and seasons.



368

369 **Figure 7. The (a) 1<sup>st</sup> and (b) 2<sup>nd</sup> important meteorological parameters (1<sup>st</sup> MET and 2<sup>nd</sup> MET, respectively) for climate-induced  
370 MDA8 O<sub>3</sub> changes in China and their relative contributions in DJF and JJA. All 1<sup>st</sup> MET and 2<sup>nd</sup> MET in each 2° × 2.5° grid cell  
371 are statistically significantly correlated with MDA8 O<sub>3</sub> ( $p < 0.05$ ). The overlaid fill patterns represent the relative contribution of the  
372 meteorological variable at this grid.**

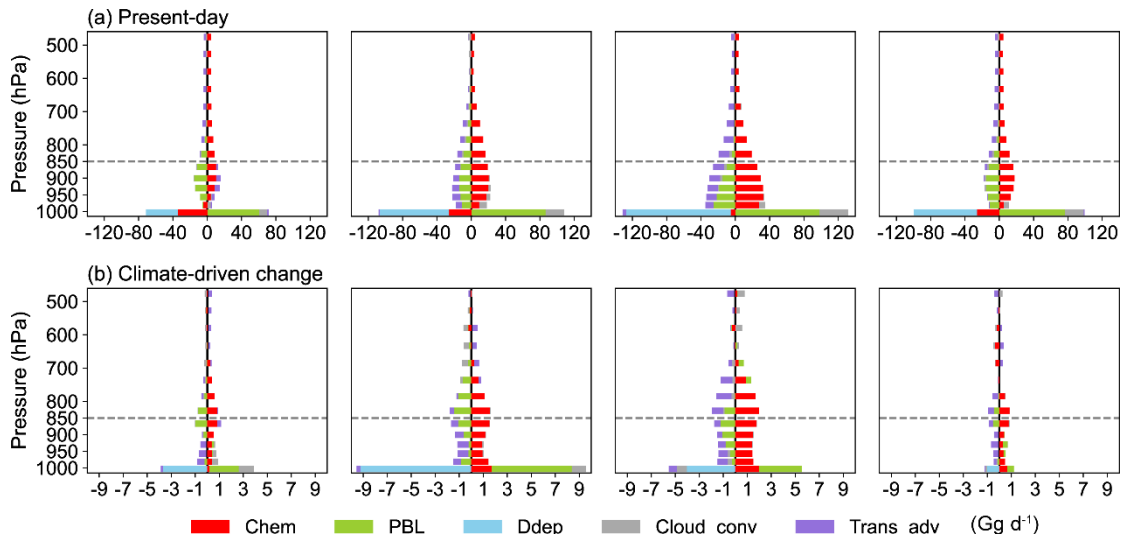
373 **3.3.2 Key processes for climate-induced O<sub>3</sub> changes**

374 We performed IPR analysis to understand the intrinsic mechanism of the impact of climate change on O<sub>3</sub> in EC. Figure 8  
375 show the vertical profiles of present-day seasonal mean O<sub>3</sub> mass and climate-driven O<sub>3</sub> mass changes of five processes (net  
376 chemical production, PBL mixing, dry deposition, cloud convection, and horizontal and vertical advection transport) in EC.  
377 Since surface O<sub>3</sub> concentrations are determined by the processes within the boundary layer (Gong and Liao, 2019), we also  
378 listed in Table 5 the present-day O<sub>3</sub> budget of five processes in EC within the boundary layer and the climate-driven O<sub>3</sub> budget  
379 changes by each process.

380 In present-day (Fig. 8a), net chemical production is negative at the surface due to the O<sub>3</sub> titration effect by abundant NO<sub>x</sub>  
381 and is positive in the upper levels due to the decreases in NO<sub>x</sub> concentrations and the strong solar radiation (Gong and Liao,  
382 2019). PBL mixing refers to O<sub>3</sub> mass fluxes by turbulence within the boundary layer, which transports O<sub>3</sub> based on the  
383 concentration gradient. Since O<sub>3</sub> concentrations are higher in the upper boundary layers than at the surface (Fig. S2), PBL  
384 mixing leads to the decreases in O<sub>3</sub> in upper layers (950 to 800 hPa) and increases in surface-layer O<sub>3</sub> levels. Dry deposition  
385 occurs only at the surface, with the values of -122.1 to -37.5 Gg d<sup>-1</sup> in different seasons. Cloud convection process in GEOS-

386 Chem model describes the redistribution of species concentrations due to upward convection inside the cumulus and  
 387 subsidence outside the cumulus. Cloud convection has a large positive value below 950 hPa in all seasons due to the frequent  
 388 non-precipitation shallow convection in GISS-E2.1 (Wu et al., 2007; Miller et al., 2021) and higher O<sub>3</sub> concentrations above  
 389 950 hPa. Horizontal and vertical advection below 850 hPa is positive in DJF and negative in other seasons. For the present-  
 390 day O<sub>3</sub> budget within the boundary layer (Table 5,  $PC_{CpdEpd}$ ), net chemical production is the dominant process that contributes  
 391 to O<sub>3</sub> budget in JJA, MAM, and SON, with the values of 136.3, 56.5, 37.6 Gg d<sup>-1</sup>, respectively. Cloud convection has  
 392 contributions of 11.0-34.4 Gg d<sup>-1</sup> to O<sub>3</sub> budget. The horizontal and vertical advection is 0.4 Gg d<sup>-1</sup> in DJF and -23.8 to -2.7 Gg  
 393 d<sup>-1</sup> in other seasons.

394 Under the impact of climate change (Fig. 8b), net chemical production exhibits distinct increases below 850 hPa in all  
 395 seasons, especially in MAM and JJA. Increases in T2max and SW (Figs. 1a and c) result in increases in BVOC emission rates  
 396 by 0.4-2.9 10<sup>-11</sup> kg m<sup>-2</sup> s<sup>-1</sup> (Fig. S3) and in photochemical reaction rates, while decreases in RH (Fig. 1b) result in decreases in  
 397 O<sub>3</sub> destruction (Gong and Liao, 2019), which together promote the net chemical production of O<sub>3</sub>. Increase in surface O<sub>3</sub> mass  
 398 by PBL mixing indicates that more O<sub>3</sub> enters the boundary layer and mixes to the surface as a result of increased PBLH (Fig.  
 399 1d). The importance of chemical process and PBL mixing corresponds well with the 1<sup>st</sup> and 2<sup>nd</sup> MET shown in Fig. 7. Dry  
 400 deposition removes more O<sub>3</sub> due to the increases in net chemical production of O<sub>3</sub>. Cloud convection increases near-surface  
 401 O<sub>3</sub> mass in DJF and MAM but decreases those in JJA. Changes in horizontal and vertical advection reduce O<sub>3</sub> mass in EC at  
 402 layers below 850 hPa. Anomalous low pressure over EC in DJF indicates the presence of anomalous upward advection (Fig.  
 403 1f). Anomalous northwesterlies over northern China in other seasons obstruct the northward transport of BVOCs from southern  
 404 China and promote the outflow of O<sub>3</sub> and its precursors from EC. Circulation changes have an important effect on JJA O<sub>3</sub>  
 405 concentrations, which are also confirmed by the 1<sup>st</sup> and 2<sup>nd</sup> MET (RH or WS850) in southern EC (Fig. 7).



406  
 407 **Figure 8. (a) Vertical profile of seasonal mean O<sub>3</sub> mass (Gg d<sup>-1</sup>) by five processes (bottom axis: net chemical production (Chem),  
 408 PBL mixing (PBL), dry deposition (Ddep), cloud convection (Cloud\_conv), and horizontal and vertical advection (Trans\_adv)) over**

409 **EC in present-day (CpdEpd), and (b) the climate-driven changes in seasonal mean O<sub>3</sub> mass of each process (CfutEpd minus CpdEpd).**  
 410 **All the panels have the same vertical axis in hPa.**

411 The sums of the climate-driven O<sub>3</sub> mass changes by all processes in EC are 0.6, 2.5, 6.5, and 1.7 Gg d<sup>-1</sup> in DJF, MAM,  
 412 JJA, and SON, respectively (Table 5,  $PC_{DIFF}$ ), which are consistent with the seasonal variations in climate-induced MDA8 O<sub>3</sub>  
 413 (Fig. 4). The net chemical production, dry deposition, and horizontal and vertical advection change by 3.3 to 16.4, -9.3 to -1.0,  
 414 and -4.3 to -0.8 Gg d<sup>-1</sup> in different seasons, respectively. The cloud convection increases by 1.5 Gg d<sup>-1</sup> in DJF and MAM and  
 415 decrease by 1.0 Gg d<sup>-1</sup> in JJA. Considering the relative contributions of individual processes (Table 5, % $PC_{DIFF}$ ), net chemical  
 416 production is the most important process contributing to the increases of O<sub>3</sub> mass in all seasons, with the relative contribution  
 417 of 34.0-62.5%. Horizontal and vertical advection in JJA (-16.6%) or dry deposition in other seasons (-37.9% to -13.7%) is the  
 418 major process that reduces O<sub>3</sub> mass as the O<sub>3</sub> mass increases from chemical reactions.

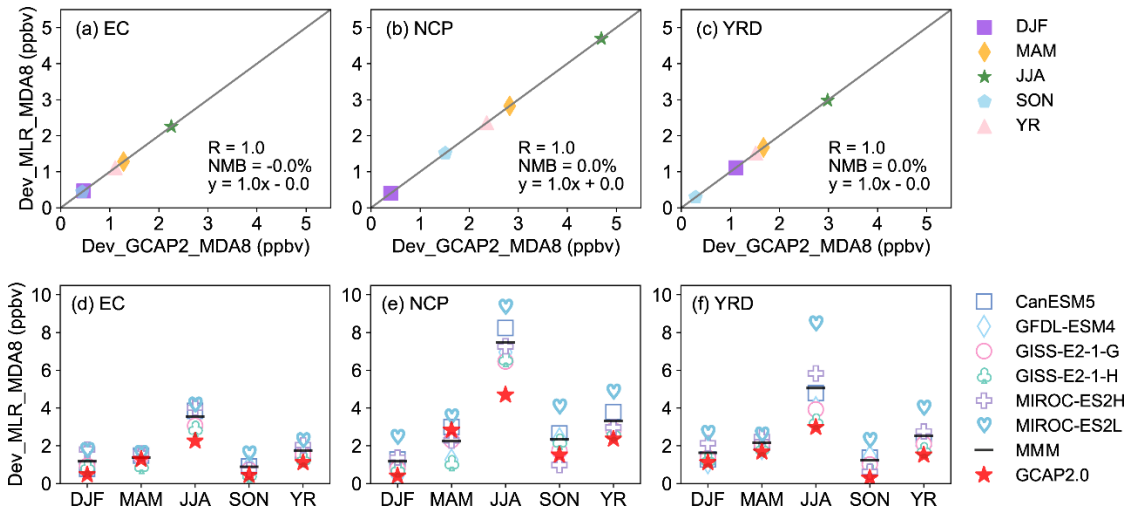
419 **Table 5. Seasonal mean O<sub>3</sub> budgets (Gg d<sup>-1</sup>) within the boundary layer over EC in CpdEpd ( $PC_{CpdEpd}$ ) and CfutEpd ( $PC_{CfutEpd}$ ).**  
 420 **The climate-driven O<sub>3</sub> budget changes of five process ( $PC_{DIFF}$ ), and the relative contribution of each process to the total O<sub>3</sub> mass  
 421 changes (% $PC_{DIFF}$ , %) are also listed, following Eqs. (2) and (3) described in Sect. 2.3.2.**

Season		Chemistry	PBL	Dry	Cloud	Advection	Total
		mixing	deposition	convection	transport		
DJF	$PC_{CpdEpd}$	-12.02	47.58	-37.46	11.01	0.39	9.50
	$PC_{CfutEpd}$	-8.74	47.93	-41.11	12.52	-0.46	10.13
	$PC_{DIFF}$	3.28	0.34	-3.65	1.51	-0.85	0.64
	% $PC_{DIFF}$	34.04	3.56	-37.88	15.71	-8.80	/
MAM	$PC_{CpdEpd}$	56.48	50.39	-80.71	25.83	-11.43	40.56
	$PC_{CfutEpd}$	68.13	50.84	-89.96	27.37	-13.35	43.03
	$PC_{DIFF}$	11.65	0.45	-9.25	1.54	-1.92	2.47
	% $PC_{DIFF}$	46.95	1.81	-37.28	6.21	-7.75	/
JJA	$PC_{CpdEpd}$	136.26	35.23	-122.07	34.37	-23.78	60.01
	$PC_{CfutEpd}$	152.61	34.75	-126.09	33.41	-28.13	66.55
	$PC_{DIFF}$	16.35	-0.48	-4.03	-0.96	-4.34	6.54
	% $PC_{DIFF}$	62.49	-1.84	-15.39	-3.67	-16.59	/
SON	$PC_{CpdEpd}$	37.58	41.58	-73.96	22.75	-2.71	25.23
	$PC_{CfutEpd}$	41.99	40.61	-74.95	22.82	-3.50	26.97
	$PC_{DIFF}$	4.42	-0.97	-0.99	0.07	-0.79	1.74
	% $PC_{DIFF}$	61.02	-13.45	-13.65	0.97	-10.90	/

422 3.4 Projections of climate-driven MDA8 O<sub>3</sub> changes from the CMIP6 models

423 In Sect. 3.3.1, we applied the stepwise MLR model to relate 10 yr daily MDA8 O<sub>3</sub> anomalies to 10 yr daily meteorological  
424 parameter anomalies at each grid cell and obtained the corresponding MLR equation. The climate-driven seasonal mean MDA8  
425 O<sub>3</sub> concentration changes projected by stepwise MLR model at each grid cell can be obtained by substituting the corresponding  
426 seasonal mean meteorological parameter anomalies of GCAP 2.0 into the regression equations obtained by daily anomalies  
427 above, which will be referred to as Dev\_MLR\_MDA8 hereafter. The Dev\_MLR\_MDA8 values for a target region are then  
428 obtained by averaging over all the grid cells in the region. We selected EC, NCP, and YRD as the target regions in this study.  
429 Figures 9a-c evaluate the seasonal and annual mean Dev\_MLR\_MDA8 values averaged over EC, NCP, and YRD by  
430 comparing them with the simulated values by GCAP 2.0 (hereafter called Dev\_GCAP2\_MDA8). The seasonal and annual  
431 mean values of Dev\_MLR\_MDA8 and Dev\_GCAP2\_MDA8 are exactly the same, with the R value of 1.0 and the NMB value  
432 of 0.0% in all three regions. In China, the spatial distributions and magnitudes of the seasonal mean Dev\_MLR\_MDA8 values  
433 are consistent with the seasonal mean Dev\_GCAP2\_MDA8 values (Fig. S4), with high pattern correlation coefficients of 1.0  
434 in four seasons, indicating that it is feasible to predict climate-driven MDA8 O<sub>3</sub> concentration changes by stepwise MLR model.  
435 Therefore, we input the corresponding seasonal mean meteorological parameter anomalies from the six CMIP6 models into  
436 the regression equations to obtain multi-model projections of climate-induced MDA8 O<sub>3</sub> changes under carbon neutrality  
437 scenario.

438 Figures 9d-f shows the climate-driven seasonal and annual mean MDA8 O<sub>3</sub> changes averaged over EC, NCP, and YRD  
439 regions predicted by stepwise MLR model using meteorology anomalies from the GCAP 2.0 and other six CMIP6 models  
440 under SSP1-1.9 scenario. The Dev\_MLR\_MDA8 values of GCAP 2.0 and all six CMIP6 models are positive throughout the  
441 year in all three regions, indicating that climate change will increase MDA8 O<sub>3</sub> concentrations over polluted regions in China  
442 even under carbon neutrality scenario. Similar to the GCAP 2.0 results, the Dev\_MLR\_MDA8 values of all six CMIP6 models  
443 in the three regions are much larger in JJA than in other seasons, with the values in the range of 2.9-4.2, 6.5-9.4, and 3.3-8.5  
444 ppbv in EC, NCP, and YRD, respectively. In JJA, the Dev\_MLR\_MDA8 values of MMM (average of six CMIP6 models) are  
445 3.5, 7.5, and 5.1 ppbv in EC, NCP, and YRD, respectively, higher than the Dev\_MLR\_MDA8 values of GCAP 2.0 of 2.3, 4.7,  
446 and 3.0 ppbv, respectively. In other seasons, the Dev\_MLR\_MDA8 values of MMM are in the range of 0.9-1.4, 1.2-2.3, and  
447 1.2-2.2 ppbv in EC, NCP, and YRD, respectively, and the Dev\_MLR\_MDA8 values of GCAP 2.0 are in the range of 0.4-1.3,  
448 0.4-2.8, and 0.3-1.7 ppbv, respectively. Overall, the Dev\_MLR\_MDA8 values of GCAP 2.0 tend to be in the lower end of the  
449 multi-model projection results, especially in JJA. The spatial distributions of climate-driven changes in annual mean MDA8  
450 O<sub>3</sub> concentrations from GCAP 2.0 and the other six CMIP6 models are shown in Fig. S5. The climate-induced increases in  
451 annual mean MDA8 O<sub>3</sub> predicted by all models are mainly concentrated in central and northern EC. In NCP and its surrounding  
452 areas, while the maximum increases in annual mean MDA8 O<sub>3</sub> concentrations were simulated to be 2-4 ppbv from GCAP 2.0,  
453 the values were 4-8 ppbv from four of the six CMIP6 models.



454

455 **Figure 9.** (a)-(c) The scatterplot of climate-induced MDA8 O<sub>3</sub> changes (ppbv) simulated by GCAP 2.0 (Dev\_GCAP2\_MDA8) versus  
 456 those projected by MLR model (Dev\_MLR\_MDA8) in EC, NCP, and YRD regions. The correlation coefficient (R), normalized mean  
 457 biases (NMB), and linear fit (grey solid line and equation) are also shown. (d)-(f) The climate-driven seasonal and annual mean  
 458 MDA8 O<sub>3</sub> concentration changes (ppbv) projected by MLR model using the climate outputs from GCAP 2.0 and six CMIP6 models  
 459 under SSP1-1.9 scenario. The multi-model mean (MMM) is calculated from the average of the six CMIP6 models. Different markers  
 460 represent different models, black lines represent MMM, and red stars represent GCAP 2.0 results.

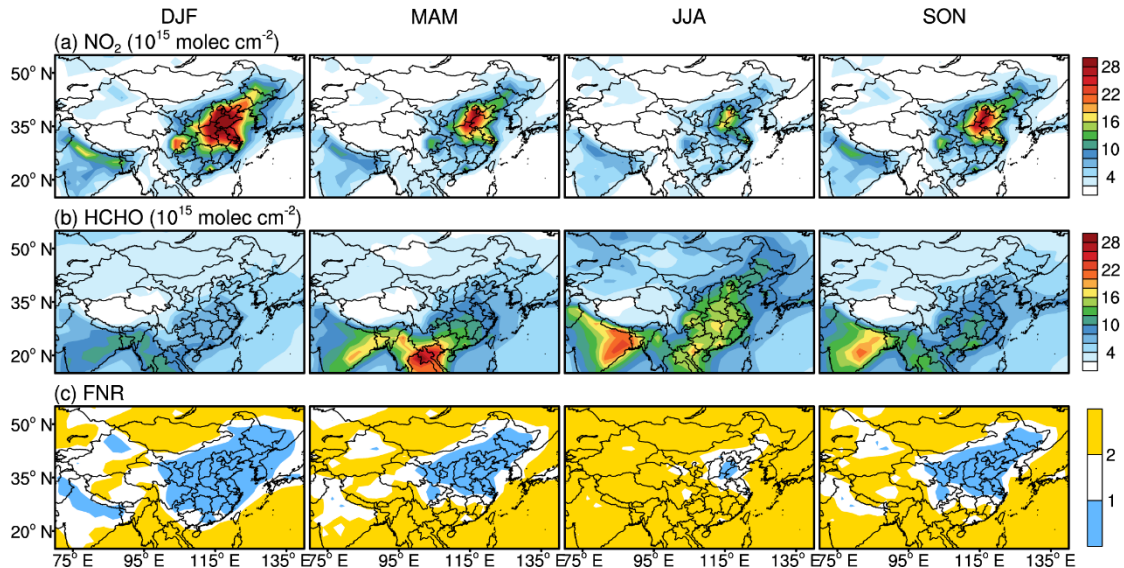
### 461 3.5 Future changes in tropospheric O<sub>3</sub> driven by changes in anthropogenic emissions

462 We show large impact of climate change on tropospheric O<sub>3</sub> in previous sections, so it is of interest to examine briefly the  
 463 effects of emission changes on surface O<sub>3</sub> levels (CpdEfut minus CpdEpd) under carbon neutrality scenario as shown in Fig.  
 464 4b. Emission change alone leads to decreases in MDA8 O<sub>3</sub> concentrations of 0.5 (1.6%), 8.0 (16.7%), 15.8 (27.1%), and 7.0  
 465 ppbv (16.5%) over EC in DJF, MAM, JJA, and SON, respectively. Although the regional mean MDA8 O<sub>3</sub> concentrations in  
 466 EC decrease in all seasons, the nationwide decreases in MDA8 O<sub>3</sub> concentration occur only in JJA. In other seasons, MDA8  
 467 O<sub>3</sub> concentrations in northern China increase owing to changes in anthropogenic emissions, with the maximum increases of 8-  
 468 12 ppbv in DJF. The regional mean MDA8 O<sub>3</sub> concentrations in NCP increase by 6.7 (34.3%) in DJF and 2.2 ppbv (6.7%) in  
 469 SON, and those in YRD increase by 3.0 ppbv (9.5%) in DJF.

470 The increases in MDA8 O<sub>3</sub> concentrations by changes in anthropogenic emissions under carbon neutrality scenario can  
 471 be explained by O<sub>3</sub> formation regime. Figure 10 shows the present-day seasonal mean formaldehyde nitrogen ratio (FNR),  
 472 which was introduced by Jin and Holloway (2015) to show O<sub>3</sub> sensitivity to its precursors (see S1 in Supplementary Material).  
 473 In DJF, FNR values in eastern China are lower than 1, indicating a general VOC-limited regime. In MAM and SON, the VOC-  
 474 limited regime shrinks toward the North China, and South China is in the NO<sub>x</sub>-limited (FNR values exceeding 2) or transitional  
 475 (FNR values between 1 and 2) regime. In JJA, most of China is in the NO<sub>x</sub>-limited regime, while the NCP region is still in the  
 476 VOC-limited or transitional regime. Although the anthropogenic emissions of VOCs and NO<sub>x</sub> in NCP decrease largely (70-

477 90%) under SSP1-1.9 scenario (Fig. S6), MDA8 O<sub>3</sub> concentrations in this region increase in the future in DJF, MAM, and  
478 SON because NCP is in the VOC-limited regime.

479 Overall, considering the combined effects of climate change and emission change (CfutEfut minus CpdEpd) (Fig. 4c),  
480 the spatial distributions and magnitudes of MDA8 O<sub>3</sub> changes are similar to those considering the emission changes alone (Fig.  
481 4b), indicating that future MDA8 O<sub>3</sub> concentrations are dominated by emission changes. However, the effects of climate  
482 penalty (0.5-2.3, 0.4-4.7, and 0.3-3.0 ppbv in EC, NCP, and YRD, respectively) cannot be ignored. Note that the sum of the  
483 individual effects of climate (Fig. 4a) and emissions (Fig. 4b) is not equal to the combined effects (Fig. 4c) due to the nonlinear  
484 relationship between the simulations (Dang et al., 2021). Additionally, it is worth noting that changes in both climate and  
485 emissions lead to increases in MDA8 O<sub>3</sub> in DJF and SON over NCP and in DJF over YRD, calling for more attention to these  
486 regions in future O<sub>3</sub> pollution control strategies.



487  
488 **Figure 10. Distributions of seasonal mean tropospheric columns of (a) nitrogen dioxide (NO<sub>2</sub>) and (b) formaldehyde (HCHO) (10<sup>15</sup>  
489 molec cm<sup>-2</sup>), and (c) formaldehyde nitrogen ratio (FNR) in present-day.**

#### 490 4 Conclusions

491 In this study, we quantify the effects of climate changes over 2010-2045 on O<sub>3</sub> levels in China under carbon neutrality  
492 scenario (SSP1-1.9 scenario), focusing on the key meteorological parameters and processes for understanding the climate-  
493 induced O<sub>3</sub> changes by using the GCAP 2.0, stepwise MLR model, LMG method, and IPR analysis. The uncertainties in future  
494 O<sub>3</sub> levels resulted from the uncertainties in simulated future climate are also quantified by using outputs of climate from CMIP6  
495 models.

496 Under carbon neutrality scenario, over EC, GCAP 2.0 and all six CMIP6 models project the increases in T2max, SW,  
497 and PBLH in all seasons, and most models project reductions in RH and SLP and increases in PREC. Projected annual mean  
498 changes over EC in T2max, SW, PBLH, PREC, RH, and SLP are, respectively, 1.4 K,  $11.8 \text{ W m}^{-2}$ , 30.6 m, 0.3 mm day $^{-1}$ , -  
499 0.7%, and -0.3 hPa on a multi-model mean (MMM) basis and 1.1 K,  $7.3 \text{ W m}^{-2}$ , 23.7 m, 0.03 mm day $^{-1}$ , -1.3%, and -0.3 hPa  
500 from GCAP 2.0. Relative to the MMM, GCAP 2.0 underestimates the increases in T2max, SW, PBLH, and PREC and  
501 overestimates the decreases in RH.

502 The GCAP 2.0 model generally reproduces the spatial distribution and magnitude of observed seasonal mean MDA8 O<sub>3</sub>  
503 concentrations, with R values of 0.12-0.63 and NMB values of 7.1-18.6% in different seasons. Climate change over 2010-  
504 2045 under the carbon neutrality scenario is simulated by GCAP 2.0 to increase the regional mean MDA8 O<sub>3</sub> concentrations  
505 by 0.4-2.3 ppbv (1.0-3.9%) over EC, 0.4-4.7 ppbv (2.0-7.3%) over NCP, and 0.3-3.0 ppbv (0.6-5.1%) over YRD in different  
506 seasons, with the maximum increases in JJA. By using the stepwise MLR model, we find that changes in the key meteorological  
507 variables retained in MLR equations can explain 58-76% of the climate-driven MDA8 O<sub>3</sub> concentration changes over EC. By  
508 using the LMG method, we find that the most important meteorological parameters for climate-induced MDA8 O<sub>3</sub> changes  
509 are not only temperature, but also SW, RH, and PBLH, depending on locations and seasons. Corresponding to these changes  
510 in meteorological parameters, IPR analysis shows that net chemical production (accounting for 34.0-62.5% of total O<sub>3</sub> mass  
511 change caused by all processes within the boundary layer) is the most important process contributing to the climate-induced  
512 increases of O<sub>3</sub> mass in all seasons. Horizontal and vertical advection in JJA (-16.6%) or dry deposition in other seasons (-  
513 37.9% to -13.7%) is the major process that reduces O<sub>3</sub> mass.

514 Under carbon neutrality scenario, future MDA8 O<sub>3</sub> concentration changes in EC are dominated by changes in  
515 anthropogenic emissions (decrease by 0.5-15.8 ppbv), however, the effects of climate penalty (increase by 0.5-2.3 ppbv from  
516 GCAP 2.0) cannot be ignored. Both climate changes and emission changes increase MDA8 O<sub>3</sub> values in DJF and SON over  
517 NCP and in DJF over YRD, indicating that these regions require more attention in future O<sub>3</sub> pollution control.

518 The estimate of the effect of climate change on O<sub>3</sub> pollution by using a single model GCAP 2.0 may have uncertainties.  
519 Therefore, we also obtain the multi-model projection results of future MDA8 O<sub>3</sub> changes driven by 2010-2045 climate change  
520 under carbon neutrality scenario by using stepwise MLR model. In JJA, six CMIP6 models project increases in MDA8 O<sub>3</sub>  
521 ranging from 2.9-4.2, 6.5-9.4, and 3.3-8.5 ppbv in EC, NCP, and YRD, respectively, indicating that GCAP 2.0 results (2.3,  
522 4.7, and 3.0 ppbv) are in the lower end of the multi-model projections. **Additionally, MDA8 O<sub>3</sub> concentrations increase by**  
523 **changes in anthropogenic emissions in the future in DJF, MAM, and SON despite the large reductions in NO<sub>x</sub> and VOCs (70-**  
524 **90%) in North China (Fig. S6) under SSP1-1.9 scenario, indicating an urgent need to find appropriate emission reduction ratios**  
525 **of VOCs and NO<sub>x</sub> based on O<sub>3</sub> sensitivity to precursors and to climate for effective future O<sub>3</sub> pollution control in China.**

526 **Data availability**

527 The observed hourly surface O<sub>3</sub> concentrations in 2015 are derived from the China National Environmental Monitoring Center  
528 (<https://air.cnemc.cn:18007/>, CNEMC). The satellite observations of NO<sub>2</sub> and HCHO are downloaded from  
529 <https://www.temis.nl/airpollution/>. The climate outputs from GCAP 2.0 and other six CMIP6 models can be downloaded from  
530 <http://atmos.earth.rochester.edu/input/gc/ExtData/GCAP2/CMIP6/> and <https://esgf-node.llnl.gov/search/cmip6/>, respectively.  
531 The GEOS-Chem model is available at [http://wiki.seas.harvard.edu/geos-chem/index.php/GEOS-Chem\\_13.2.1](http://wiki.seas.harvard.edu/geos-chem/index.php/GEOS-Chem_13.2.1). The  
532 anthropogenic and biomass burning emission inventory of SSP1-1.9 are available from  
533 <https://aims2.llnl.gov/search/input4mips/>. The simulation results are available upon request from the corresponding author  
534 ([hongliao@nuist.edu.cn](mailto:hongliao@nuist.edu.cn)).

535 **Author contributions**

536 LK and HL conceived the study and designed the experiments. LK carried out the model simulations and performed the data  
537 analysis. KL, XY, YY, and YW provided useful comments on the paper. LK and HL prepared the paper.  
538

539 **Competing interests**

540 The authors declare that they have no conflict of interest.

541 **Acknowledgements**

542 We acknowledge the CNEMC, Tropospheric Emission Monitoring Internet Service (TEMIS), and CMIP6 teams for making  
543 their data publicly available. We acknowledge the efforts of GEOS-Chem working groups for developing and managing the  
544 model.

545 **Financial support**

546 This work was supported by the National Natural Science Foundation of China under grants 42293320 and 42021004.

547 **References**

548 Ainsworth, E. A., Lemonnier, P., and Wedow, J. M.: The influence of rising tropospheric carbon dioxide and ozone on plant  
549 productivity, *Plant Biol.*, 22, 5-11, <https://doi.org/10.1111/plb.12973>, 2020.

550 Bey, I., Jacob, D. J., Yantosca, R. M., Logan, J. A., Field, B. D., Fiore, A. M., Li, Q. B., Liu, H. Y., Mickley, L. J., and Schultz,  
551 M. G.: Global modeling of tropospheric chemistry with assimilated meteorology: Model description and evaluation, *J.*  
552 *Geophys. Res.*, 106, 23073-23095, <https://doi.org/10.1029/2001jd000807>, 2001.

553 Bhattacharai, H., Tai, A. P. K., Val Martin, M., and Yung, D. H. Y.: Impacts of changes in climate, land use, and emissions on  
554 global ozone air quality by mid-21st century following selected Shared Socioeconomic Pathways, *Sci. Total Environ.*, 906,  
555 <https://doi.org/10.1016/j.scitotenv.2023.167759>, 2024.

556 Checa-Garcia, R., Hegglin, M. I., Kinnison, D., Plummer, D. A., and Shine, K. P.: Historical Tropospheric and Stratospheric  
557 Ozone Radiative Forcing Using the CMIP6 Database, *Geophys. Res. Lett.*, 45, 3264-3273,  
558 <https://doi.org/10.1002/2017gl076770>, 2018.

559 Dai, H., Liao, H., Li, K., Yue, X., Yang, Y., Zhu, J., Jin, J., Li, B., and Jiang, X.: Composited analyses of the chemical and  
560 physical characteristics of co-polluted days by ozone and PM<sub>2.5</sub> over 2013–2020 in the Beijing–Tianjin–Hebei region, *Atmos.*  
561 *Chem. Phys.*, 23, 23-39, <https://doi.org/10.5194/acp-23-23-2023>, 2023.

562 Dang, R. and Liao, H.: Radiative Forcing and Health Impact of Aerosols and Ozone in China as the Consequence of Clean Air  
563 Actions over 2012–2017, *Geophys. Res. Lett.*, 46, 12511-12519, <https://doi.org/10.1029/Radiative>, 2019a.

564 Dang, R. and Liao, H.: Severe winter haze days in the Beijing–Tianjin–Hebei region from 1985 to 2017 and the roles of  
565 anthropogenic emissions and meteorology, *Atmos. Chem. Phys.*, 19, 10801-10816, <https://doi.org/10.5194/acp-19-10801-2019>, 2019b.

566 Dang, R., Liao, H., and Fu, Y.: Quantifying the anthropogenic and meteorological influences on summertime surface ozone in  
567 China over 2012-2017, *Sci. Total Environ.*, 754, 142394, <https://doi.org/10.1016/j.scitotenv.2020.142394>, 2021.

568 Eastham, S. D., Weisenstein, D. K., and Barrett, S. R. H.: Development and evaluation of the unified tropospheric–  
569 stratospheric chemistry extension (UCX) for the global chemistry-transport model GEOS-Chem, *Atmos. Environ.*, 89, 52-63,  
570 <https://doi.org/10.1016/j.atmosenv.2014.02.001>, 2014.

571 Gidden, M. J., Riahi, K., Smith, S. J., Fujimori, S., Luderer, G., Kriegler, E., van Vuuren, D. P., van den Berg, M., Feng, L.,  
572 Klein, D., Calvin, K., Doelman, J. C., Frank, S., Fricko, O., Harmsen, M., Hasegawa, T., Havlik, P., Hilaire, J., Hoesly, R.,  
573 Horing, J., Popp, A., Stehfest, E., and Takahashi, K.: Global emissions pathways under different socioeconomic scenarios for  
574 use in CMIP6: a dataset of harmonized emissions trajectories through the end of the century, *Geosci. Model Dev.*, 12, 1443-  
575 1475, <https://doi.org/10.5194/gmd-12-1443-2019>, 2019.

576 Gong, C. and Liao, H.: A typical weather pattern for ozone pollution events in North China, *Atmos. Chem. Phys.*, 19, 13725-  
577 13740, <https://doi.org/10.5194/acp-19-13725-2019>, 2019.

578 Gong, C., Liao, H., Zhang, L., Yue, X., Dang, R., and Yang, Y.: Persistent ozone pollution episodes in North China exacerbated  
579 by regional transport, *Environ. Pollut.*, 265, 115056, <https://doi.org/10.1016/j.envpol.2020.115056>, 2020.

580 Gong, C., Wang, Y., Liao, H., Wang, P., Jin, J., and Han, Z.: Future Co-Occurrences of Hot Days and Ozone-Polluted Days  
581 Over China Under Scenarios of Shared Socioeconomic Pathways Predicted Through a Machine-Learning Approach, *Earth's*  
582 *Future*, 10, <https://doi.org/10.1029/2022ef002671>, 2022.

584 Grömping, U.: Relative Importance for Linear Regression in R: The Package *relaimpo*, *Journal of Statistical Software*, 17, 1-  
585 27, <https://doi.org/10.18637/jss.v017.i01>, 2006.

586 Grulke, N. E. and Heath, R. L.: Ozone effects on plants in natural ecosystems, *Plant Biol.*, 22 12-37,  
587 <https://doi.org/10.1111/plb.12971>, 2020.

588 Hong, C., Zhang, Q., Zhang, Y., Davis, S. J., Tong, D., Zheng, Y., Liu, Z., Guan, D., He, K., and Schellnhuber, H. J.: Impacts  
589 of climate change on future air quality and human health in China, *Proc. Natl. Acad. Sci. USA*, 116, 17193-17200,  
590 <https://doi.org/10.1073/pnas.1812881116>, 2019.

591 Jin, X. and Holloway, T.: Spatial and temporal variability of ozone sensitivity over China observed from the Ozone Monitoring  
592 Instrument, *J. Geophys. Res.: Atmos.*, 120, 7229-7246, <https://doi.org/10.1002/2015jd023250>, 2015.

593 Kelley, M., Schmidt, G. A., Nazarenko, L. S., Bauer, S. E., Ruedy, R., Russell, G. L., Ackerman, A. S., Aleinov, I., Bauer, M.,  
594 Bleck, R., Canuto, V., Cesana, G., Cheng, Y., Clune, T. L., Cook, B. I., Cruz, C. A., Del Genio, A. D., Elsaesser, G. S.,  
595 Faluvegi, G., Kiang, N. Y., Kim, D., Lacis, A. A., Leboissetier, A., LeGrande, A. N., Lo, K. K., Marshall, J., Matthews, E. E.,  
596 McDermid, S., Mezuman, K., Miller, R. L., Murray, L. T., Oinas, V., Orbe, C., Garcia-Pando, C. P., Perlwitz, J. P., Puma, M.  
597 J., Rind, D., Romanou, A., Shindell, D. T., Sun, S., Tausnev, N., Tsigaridis, K., Tselioudis, G., Weng, E., Wu, J., and Yao, M.  
598 S.: GISS-E2.1: Configurations and Climatology, *J. Adv. Model. Earth Syst.*, 12, e2019MS002025,  
599 <https://doi.org/10.1029/2019MS002025>, 2020.

600 Li, A., Zhou, Q., and Xu, Q.: Prospects for ozone pollution control in China: An epidemiological perspective, *Environ. Pollut.*,  
601 285, 117670, <https://doi.org/10.1016/j.envpol.2021.117670>, 2021.

602 Li, H., Yang, Y., Jin, J., Wang, H., Li, K., Wang, P., and Liao, H.: Climate-driven deterioration of future ozone pollution in  
603 Asia predicted by machine learning with multi-source data, *Atmos. Chem. Phys.*, 23, 1131-1145, <https://doi.org/10.5194/acp-23-1131-2023>, 2023.

604 Li, K., Jacob, D. J., Liao, H., Shen, L., Zhang, Q., and Bates, K. H.: Anthropogenic drivers of 2013-2017 trends in summer  
605 surface ozone in China, *Proc. Natl. Acad. Sci. USA*, 116, 422-427, <https://doi.org/10.1073/pnas.1812168116>, 2019.

606 Li, K., Jacob, D. J., Shen, L., Lu, X., De Smedt, I., and Liao, H.: Increases in surface ozone pollution in China from 2013 to  
607 2019: anthropogenic and meteorological influences, *Atmos. Chem. Phys.*, 20, 11423-11433, <https://doi.org/10.5194/acp-20-11423-2020>, 2020.

608 Lin, J.-T. and McElroy, M. B.: Impacts of boundary layer mixing on pollutant vertical profiles in the lower troposphere:  
609 Implications to satellite remote sensing, *Atmos. Environ.*, 44, 1726-1739, <https://doi.org/10.1016/j.atmosenv.2010.02.009>,  
610 2010.

611 Liu, Q., Lam, K. S., Jiang, F., Wang, T. J., Xie, M., Zhuang, B. L., and Jiang, X. Y.: A numerical study of the impact of climate  
612 and emission changes on surface ozone over South China in autumn time in 2000–2050, *Atmos. Environ.*, 76, 227-237,  
613 <https://doi.org/10.1016/j.atmosenv.2013.01.030>, 2013.

614 Lou, S., Liao, H., and Zhu, B.: Impacts of aerosols on surface-layer ozone concentrations in China through heterogeneous  
615 reactions and changes in photolysis rates, *Atmos. Environ.*, 85, 123-138, <https://doi.org/10.1016/j.atmosenv.2013.12.004>, 2014.

618 Lu, X., Zhang, L., Wang, X., Gao, M., Li, K., Zhang, Y., Yue, X., and Zhang, Y.: Rapid Increases in Warm-Season Surface  
619 Ozone and Resulting Health Impact in China Since 2013, *Environ. Sci. Technol. Lett.*, 7, 240-247,  
620 <https://doi.org/10.1021/acs.estlett.0c00171>, 2020.

621 Miller, R. L., Schmidt, G. A., Nazarenko, L. S., Bauer, S. E., Kelley, M., Ruedy, R., Russell, G. L., Ackerman, A. S., Aleinov,  
622 I., Bauer, M., Bleck, R., Canuto, V., Cesana, G., Cheng, Y., Clune, T. L., Cook, B. I., Cruz, C. A., Del Genio, A. D., Elsaesser,  
623 G. S., Faluvegi, G., Kiang, N. Y., Kim, D., Lacis, A. A., Leboissetier, A., LeGrande, A. N., Lo, K. K., Marshall, J., Matthews,  
624 E. E., McDermid, S., Mezuman, K., Murray, L. T., Oinas, V., Orbe, C., Pérez García-Pando, C., Perlitz, J. P., Puma, M. J.,  
625 Rind, D., Romanou, A., Shindell, D. T., Sun, S., Tausnev, N., Tsigaridis, K., Tselioudis, G., Weng, E., Wu, J., and Yao, M.  
626 S.: CMIP6 Historical Simulations (1850–2014) With GISS-E2.1, *J. Adv. Model. Earth Syst.*, 13,  
627 <https://doi.org/10.1029/2019ms002034>, 2021.

628 Mu, Q. and Liao, H.: Simulation of the interannual variations of aerosols in China: role of variations in meteorological  
629 parameters, *Atmos. Chem. Phys.*, 14, 9597-9612, <https://doi.org/10.5194/acp-14-9597-2014>, 2014.

630 Murray, L. T., Leibensperger, E. M., Orbe, C., Mickley, L. J., and Sulprizio, M.: GCAP 2.0: a global 3-D chemical-transport  
631 model framework for past, present, and future climate scenarios, *Geosci. Model Dev.*, 14, 5789-5823,  
632 <https://doi.org/10.5194/gmd-14-5789-2021>, 2021.

633 Pye, H. O. T., Liao, H., Wu, S., Mickley, L. J., Jacob, D. J., Henze, D. K., and Seinfeld, J. H.: Effect of changes in climate and  
634 emissions on future sulfate-nitrate-ammonium aerosol levels in the United States, *J. Geophys. Res.: Atmos.*, 114,  
635 <https://doi.org/10.1029/2008jd010701>, 2009.

636 Riahi, K., van Vuuren, D. P., Kriegler, E., Edmonds, J., O'Neill, B. C., Fujimori, S., Bauer, N., Calvin, K., Dellink, R., Fricko,  
637 O., Lutz, W., Popp, A., Cuaresma, J. C., Kc, S., Leimbach, M., Jiang, L., Kram, T., Rao, S., Emmerling, J., Ebi, K., Hasegawa,  
638 T., Havlik, P., Humpenöder, F., Da Silva, L. A., Smith, S., Stehfest, E., Bosetti, V., Eom, J., Gernaat, D., Masui, T., Rogelj,  
639 J., Strefler, J., Drouet, L., Krey, V., Luderer, G., Harmsen, M., Takahashi, K., Baumstark, L., Doelman, J. C., Kainuma, M.,  
640 Klimont, Z., Marangoni, G., Lotze-Campen, H., Obersteiner, M., Tabéau, A., and Tavoni, M.: The Shared Socioeconomic  
641 Pathways and their energy, land use, and greenhouse gas emissions implications: An overview, *Global Environ. Change*, 42,  
642 153-168, <https://doi.org/10.1016/j.gloenvcha.2016.05.009>, 2017.

643 Shi, X., Zheng, Y., Lei, Y., Xue, W., Yan, G., Liu, X., Cai, B., Tong, D., and Wang, J.: Air quality benefits of achieving carbon  
644 neutrality in China, *Sci. Total Environ.*, 795, <https://doi.org/10.1016/j.scitotenv.2021.148784>, 2021.

645 Tang, K., Zhang, H., Feng, W., Liao, H., Hu, J., and Li, N.: Increasing but Variable Trend of Surface Ozone in the Yangtze  
646 River Delta Region of China, *Front. Environ. Sci.*, 10, <https://doi.org/10.3389/fenvs.2022.836191>, 2022.

647 Wang, Y., Jacob, D. J., and Logan, J. A.: Global simulation of tropospheric O<sub>3</sub>-NO<sub>x</sub>-hydrocarbon chemistry: 1. Model  
648 formulation, *J. Geophys. Res.: Atmos.*, 103, 10713-10725, <https://doi.org/10.1029/98jd00158>, 1998.

649 Wang, Y., Liao, H., Chen, H., and Chen, L.: Future Projection of Mortality From Exposure to PM<sub>2.5</sub> and O<sub>3</sub> Under the Carbon  
650 Neutral Pathway: Roles of Changing Emissions and Population Aging, *Geophys. Res. Lett.*, 50,  
651 <https://doi.org/10.1029/2023gl104838>, 2023.

652 Wang, Y., Shen, L., Wu, S., Mickley, L., He, J., and Hao, J.: Sensitivity of surface ozone over China to 2000–2050 global  
653 changes of climate and emissions, *Atmos. Environ.*, 75, 374-382, <https://doi.org/10.1016/j.atmosenv.2013.04.045>, 2013.

654 Wesely, M. L.: Parameterization of surface resistances to gaseous dry deposition in regional-scale numerical models, *Atmos.*  
655 *Environ.*, 23, 1293-1304, [https://doi.org/10.1016/0004-6981\(89\)90153-4](https://doi.org/10.1016/0004-6981(89)90153-4), 1989.

656 Wu, S., Mickley, L. J., Jacob, D. J., Logan, J. A., Yantosca, R. M., and Rind, D.: Why are there large differences between  
657 models in global budgets of tropospheric ozone?, *J. Geophys. Res.: Atmos.*, 112, <https://doi.org/10.1029/2006jd007801>, 2007.

658 Xu, B., Wang, T., Ma, D., Song, R., Zhang, M., Gao, L., Li, S., Zhuang, B., Li, M., and Xie, M.: Impacts of regional emission  
659 reduction and global climate change on air quality and temperature to attain carbon neutrality in China, *Atmos. Res.*, 279,  
660 <https://doi.org/10.1016/j.atmosres.2022.106384>, 2022.

661 Yang, Y., Li, M., Wang, H., Li, H., Wang, P., Li, K., Gao, M., and Liao, H.: ENSO modulation of summertime tropospheric  
662 ozone over China, *Environ. Res. Lett.*, 17, <https://doi.org/10.1088/1748-9326/ac54cd>, 2022.

663 Yue, X., Unger, N., Harper, K., Xia, X., Liao, H., Zhu, T., Xiao, J., Feng, Z., and Li, J.: Ozone and haze pollution weakens net  
664 primary productivity in China, *Atmos. Chem. Phys.*, 17, 6073-6089, <https://doi.org/10.5194/acp-17-6073-2017>, 2017.

665 Zanis, P., Akritidis, D., Turnock, S., Naik, V., Szopa, S., Georgoulias, A. K., Bauer, S. E., Deushi, M., Horowitz, L. W., Keeble,  
666 J., Le Sager, P., O'Connor, F. M., Oshima, N., Tsigaridis, K., and van Noije, T.: Climate change penalty and benefit on surface  
667 ozone: a global perspective based on CMIP6 earth system models, *Environ. Res. Lett.*, 17, <https://doi.org/10.1088/1748-9326/ac4a34>, 2022.

668 Zhai, S., Jacob, D. J., Wang, X., Shen, L., Li, K., Zhang, Y., Gui, K., Zhao, T., and Liao, H.: Fine particulate matter (PM<sub>2.5</sub>)  
669 trends in China, 2013–2018: separating contributions from anthropogenic emissions and meteorology, *Atmos. Chem. Phys.*,  
670 19, 11031-11041, <https://doi.org/10.5194/acp-19-11031-2019>, 2019.

671 Zheng, B., Tong, D., Li, M., Liu, F., Hong, C., Geng, G., Li, H., Li, X., Peng, L., Qi, J., Yan, L., Zhang, Y., Zhao, H., Zheng,  
672 Y., He, K., and Zhang, Q.: Trends in China's anthropogenic emissions since 2010 as the consequence of clean air actions,  
673 *Atmos. Chem. Phys.*, 18, 14095-14111, <https://doi.org/10.5194/acp-18-14095-2018>, 2018.

674 Zhu, J., Yang, Y., Wang, H., Gao, J., Liu, C., Wang, P., and Liao, H.: Impacts of projected changes in sea surface temperature  
675 on ozone pollution in China toward carbon neutrality, *Sci. Total Environ.*, 915,  
676 <https://doi.org/10.1016/j.scitotenv.2024.170024>, 2024.

677

678